International Journal of Solids and Structures 249 (2022) 111628

Contents lists available at ScienceDirect

International Journal of Solids and Structures

journal homepage: www.elsevier.com/locate/ijsolstr

Fiber plasticity and loss of ellipticity in soft composites under non-monotonic loading

Fernanda F. Fontenele [a], Nelly Andarawis-Puri [a,b], Michalis Agoras [c], Nikolaos Bouklas [a,*]

[a] Sibley School of Mechanical and Aerospace Engineering, Cornell University, NY 14853, USA
[b] Hospital for Special Surgery, NY 10021, USA
[c] Department of Mechanical Engineering, University of Thessaly, 38334 Volos, Greece

ARTICLE INFO

Keywords:
Loss of ellipticity
Soft composites
Fiber kinking
Plasticity
Stability

ABSTRACT

In this work, we relate fiber plasticity in soft composites to the loss of ellipticity of the governing equations of equilibrium of a composite under non-monotonic uniaxial loading. The loss of ellipticity strongly indicates the emergence of localization phenomena in the composite, reminiscent of the emergence of kinking instabilities in tendon, which occur as a response to tendon ''overloading'' without requiring any macroscopic compressive loading. We examine soft composites where both fibers and matrix can be highly extensible and plastic deformations are present in the fiber phase. We first propose a transversely isotropic constitutive model for the fibers allowing for plastic deformation, taking into account a single slip direction, consistent with the microstructure of hierarchically assembled collagen fibers. Following, we propose a simple hyperelastic model for the matrix and combine the two following the Voigt assumption. We then formulate a general loss of ellipticity criterion for an elastoplastic material subjected to finite deformations. We use this criterion to indicate critical conditions for loss of ellipticity in the soft composite and individually in the fiber phase, under various loading–unloading paths. Results show that plastic deformation of the fiber phase during tensile loading can lead to ellipticity breakdown during elastic unloading while, macroscopically, the material is still in tension, indicating the possible onset of an instability.

1. Introduction

Recent advancements in fiber technology have led to the development of hierarchical fibers, composed of building blocks such as carbon nanotubes (CNTs), that exhibit plastic deformations to combine extensibility, strength, toughness (Beese et al., 2013) and multifunctionality (Li et al., 2018). Advanced biosynthesis approaches on the other hand have also led to the development of plastically deforming fibers from biopolymers based on collagen, silk and cellulose (Burla et al., 2020; Larsson et al., 2014; Wang et al., 2017; Ansari et al., 2014; Li et al., 2012; Wu et al., 2019). Nature's design and novel nanomaterial synthesis techniques incite the exploration of bio-inspired template for the optimization of soft fiber-reinforced composites, which dictates that the fiber phase can exhibit plastic deformations (Yodmuang et al., 2015; Cheung et al., 2008; Gea et al., 2010; Lee et al., 2012; Sehaquiet al., 2011; Callens et al., 2014). This template is followed in biological materials when high extensibility, toughness and fatigue resistance are necessary, as plastic deformation in the fiber phase leads to increased energy dissipation. More specifically, tendon and ligaments, are soft composite materials with aligned ductile collagen fibers (Baldwin et al., 2014; Veres et al., 2013, 2014) and a soft matrix. As a result of their architecture and available dissipation mechanisms, they exhibit high extensibility, toughness, and fatigue resistance as they undergo repeated loading (Freedman et al., 2014; Thorpe and Screen, 2016). This bio-inspired template is very promising for the design of the next generation of soft composite materials, with target applications in the replacement of load-bearing soft tissues (e.g. meniscus, ligament, tendon) and multifunctional tough ''ligaments'' for soft robotics (Pan et al., 2020).

In biological fiber-reinforced soft composites such as ligament and tendon, plasticity is known to occur through levels of the tendon hierarchy, and significant attention has been recently given to plasticity at the fibril level (Herod et al., 2016; Veres et al., 2014; Baldwin et al., 2016; Veres et al., 2013, 2015; Baldwin et al., 2014; Tang et al., 2010). An interesting phenomenon that has not been fully understood in tendon is fiber kinking, which is observed when tendon is unloaded upon repeated cyclic loading as seen in Fig. 1. Fiber kinking is treated as a precursor to tendon damage and its emergence is not fully understood (Andarawis-Puri et al., 2009, 2012b, a, 2015; Fung

* Corresponding author.
E-mail address: nb589@cornell.edu (N. Bouklas).

https://doi.org/10.1016/j.ijsolstr.2022.111628
Received 29 July 2021; Received in revised form 22 March 2022; Accepted 14 April 2022
Available online 11 May 2022

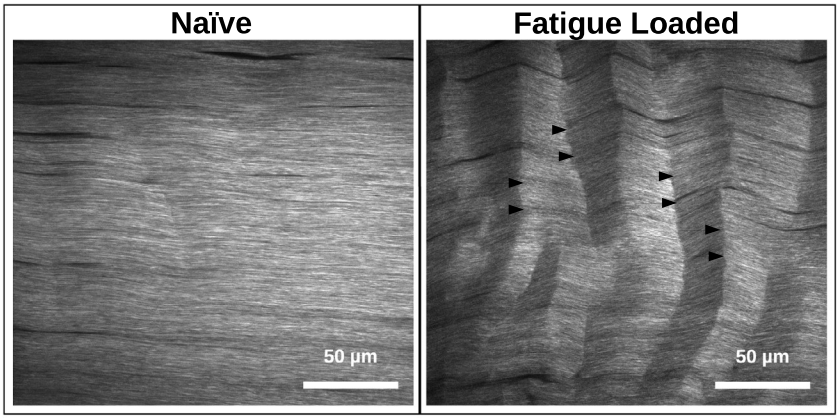

Fig. 1. Multiphoton microscopy of naive (left) and cyclically loaded (right) rat patellar tendons. Cyclic loading is conducted in uniaxial tension for 7200 cycles at 1 Hz, where each cycle peaked at 40 N (40% of the ultimate load) and images were captured in an unloaded state. The arrows in the cyclically loaded state correspond to localized deformations, often referred to as ''kinking''.

et al., 2010; Neviaser et al., 2012). Kink-band formation has also been observed extensively in the context of engineering fiber-reinforced composites, mainly under compressive loading (Budiansky and Fleck, 1994; Sivashanker et al., 1996; Berbinau et al., 1999). The damage in tendons under fatigue loads has been related to the development of diseases such as tendinopathy, see Freedman et al. (2014) and Maffulli et al. (2003). This disease has been especially associated with the late stages of accumulated tendon damage, characterized by rupture of fibers. In this context, few researchers have addressed the progression process of damage that precedes rupture, see Andarawis-Puri et al. (2009), Natali et al. (2005), Ciarletta and Ben Amar (2009), Ciarletta et al. (2008). Shen et al. (2010) studied the mechanical behavior at a fibril level of collagen of biological structures stretched in one direction and characterized the fracture into brittle or plastic. Andarawis-Puri and Flatow (2011) investigated three different levels of fatigue damage on rat tendons and noticed the formation of kinks on the tendons under lower levels of fatigue. Jozsa et al. (1984) studied collagen fibrils and found the presence of kinks in spontaneously ruptured human tendons.

Despite these contributions of the aforementioned studies, kinks were only treated as a precursor to material failure in cyclic loading, and the formation of these repeated deformation patterns was not fully analyzed. On the other hand, the understanding of the damage progression in tendons is essential for tendinopathy prognosis, and also for informing exercise-based treatments. In parallel, plasticity was observed in tendon experiments from discrete plasticity (see Veres et al. (2013, 2015), Herod et al. (2016), Veres et al. (2014), Baldwin et al. (2016, 2014)) at the fibril level which alters the morphology of the fibers to macroscopic plasticity under cyclic loading at the tendon level (see Fung et al. (2009), Andarawis-Puri et al. (2012a)). Tang et al. (2010) attempted to validate the origins of plasticity by identifying the plastic deformation mechanisms present in collagen fibrils when loaded in uniaxial tension through computational molecular dynamics modeling. Furthermore Fung et al. (2009) and Veres et al. (2013) argued that this plastic deformation of the fibers was the major cause of the formation of kinks in tendons. Understanding how multiscale mechanics of soft composites can lead to similar localization phenomena under non-monotonic loading is a crucial first step towards understanding this localization phenomenon in tendons. In this work, we aim to investigate whether plastic deformations in the fiber phase can indeed be responsible for localization in the composite under tensile loading conditions. We use the concept of loss of ellipticity to indicate critical conditions that can potentially lead to localization.

To the best of our knowledge, there is currently no theoretical work in the literature to address the effect of fiber plasticity on the macroscopic stability of soft fiber-reinforced composites. In contrast, there are numerous studies dealing with the effect of matrix plasticity on the development of instabilities and failure of polymer–matrix composites (e.g., graphite-epoxy) under compressive loading conditions along the fiber direction (see, e.g., Budiansky and Fleck (1993) and Fleck (1997)). These studies have established that the plastic deformation in the matrix has a significant effect on the compressive failure of these materials and that the dominant failure mode is localized plastic kinking (e.g., Kyriakides et al. (1995) and Vogler et al. (2000)). Given the inherent difficulties involved in the micromechanical analysis of these instabilities, following the pioneering work by Rosen (1965), several authors have utilized composite materials with lamellar microstructures as two-dimensional approximations of the fiber-reinforced composites of interest. Along these lines, a detailed investigation of microscopic and macroscopic instabilities in finitely strained elastoplastic laminates has been carried out by Triantafyllidis and co-workers (e.g., Triantafyllidis and Maker (1985) and Nestorović and Triantafyllidis (2004)). An important finding of these works is that macroscopic (long wavelength) instabilities, which may be conveniently computed from the loss of ellipticity (LOE) of the associated homogenized constitutive equations, is an upper bound to the microscopic (short wavelength) instabilities (see also Geymonat et al. (1993)). In more recent work, d'Avila et al. (2016) have shown that the LOE of the homogenized behavior of hyperelastic laminates leads to a macroscopically unstable behavior (strain localization) in certain cases, but not in others, depending crucially on the constitutive relations of the constituent phases. Furthermore, Fortier and Castañeda (2020) have demonstrated that the onset of macroscopic instabilities in neo-Hookean laminates is determined by the loss of global rank-1 convexity of the principal solution, which usually occurs before the loss of strong ellipticity and leads to the formation of microstructure (lamellar domains) at a mesoscopic length scale. In addition to the above contributions, the LOE of phenomenological, nonlinear elastic, transversely isotropic constitutive relations has been studied by several authors (e.g., Merodio and Ogden (2002), Triantafyllidis and Abeyaratne (1983), Merodio and Ogden (2003), Qiu and Pence (1997a)). Furthermore, an analysis of the onset of macroscopic instabilities in hyperelastic fiber-reinforced elastomers under general loading conditions has been carried out by Agoras et al. (2009b) by studying the LOE of the associated homogenization models of Agoras et al. (2009a) and DeBotton et al. (2006).

The motivation for this work is the fact that there is no clear mechanistic understanding of how the ubiquitous phenomenon of fiber kinking emerges in tendon due to so-called ''overload''. There have been several experimental studies on the topic, but no theoretical or computational studies have been able to provide a mechanistic interpretation of the phenomenon. In this work, we aim to investigate

the pathway that could possibly lead to a similar instability in a soft fiber-reinforced composite to emerge. More specifically, we investigate the LOE of the composite in the context of non-monotonic loading allowing for plastic deformations in the fiber phase. LOE, as mentioned previously, does not necessitate localization but in many problems indicates it. The proposed model is not a complete model of the mechanical behavior tendon, but a simple approximation that can relate to tendon as it shares some low-level common features such as a ductile stiff fiber phase corresponding to collagen fibers and a soft and elastic matrix phase corresponding to proteoglycans and elastin. The main purpose of this work is to investigate theoretically the role of fiber plasticity on the LOE in soft fiber-reinforced composites under tensile cyclic loading. To this end, we model the material of the matrix as an isotropic hyperelastic solid and that of the fibers as a transversely isotropic elastoplastic solid. Transverse isotropy is used in the fiber phase to maintain the hierarchy observed in the fiber phase itself, will be further discussed. A simple constitutive model for the macroscopic response of the composite is derived by employing a Voigt-type of approximation. The loss of ellipticity of the model under cyclic loading and the effect of fiber plasticity are discussed in detail.

The paper is organized as follows. In Section 2, we provide a general description of the problem considered in this paper, as well as an introduction on basic concepts on the kinematics of finite deformations, including the theory of multiplicative decomposition of the deformation gradient for plasticity. Additionally, in the same section, we provide an outline of the stress power relations and of the relations characterizing the elastic and the plastic behavior of a general nonlinear material, and finally, we provide a description of the incremental elastoplastic constitutive equations. In Section 3.1, we formulate the effective behavior for the soft composite with fiber plasticity considering the Voigt approximation. In Section 4, we formulate a general loss of ellipticity (LOE) condition for the incremental equations of equilibrium that can be used both at the macroscopic level of the homogenized composite and at the microscopic level of its homogeneous constituents, in the context of finite elastoplasticity. In Section 5, we discuss numerical results, where we study the thermodynamic limit of the constitutive model of the fiber phase and the composite under uniaxial elastic loading, and also investigate the onset of instabilities in the composite and individually in the fiber phase. In the Appendix, we include a discussion on how to determine the thermodynamic limit of a hyperelastic material model. We also repeat one set of the calculations shown in Section 5 for a thermodynamically stable free energy function and verify that the trend in the results of loss of ellipticity remains unaltered.

Standard notation is used throughout the article. Tensors of first, second, and fourth order are denoted by boldface letters. The components of all tensors are referred to a fixed Cartesian system defined by the orthonormal basis vectors $\mathbf{e}_i$ with $i = 1, 2, 3$, and are denoted by lightface italics. For definiteness, let $\mathbf{a}$ and $\mathbf{b}$ be vectors, $\mathbf{L}_t$ and $\mathbf{L}^{\text{fiber}}_{\text{tine}}$ second-order tensors, and $\mathbb{L}$ and $\mathbb{I}$ fourth-order tensors, with components a_i, b_i, L_{ij}, $L^{\text{fiber}}_{\text{tine}\,ij}$, $\mathbb{L}_{ijkl}$, and $\mathbb{I}_{ijkl}$, respectively. The summation convention is used throughout for repeated indices. The scalar product of any pair of tensors of the same order is denoted by a dot, e.g., we write $\mathbf{a} \cdot \mathbf{b} = a_i b_i$ and $\mathbf{L}_t \cdot \mathbf{L}^{\text{fiber}}_{\text{tine}} = L_{ij} L^{\text{fiber}}_{\text{tine}\,ij}$, whereas the dyadic product between tensor of any order is denoted by the symbol $\otimes$, e.g., $(\mathbf{a} \otimes \mathbf{b})_{ij} = a_i b_j$ and $(\mathbf{L}_t \otimes \mathbf{L}^{\text{fiber}}_{\text{tine}})_{ijkl} = L_{ij} L^{\text{fiber}}_{\text{tine}\,kl}$. We make use of no particular symbol to denote linear mappings or compositions of mappings and let their precise meaning be inferred from the context. For instance, $(\mathbf{L}^{\text{fiber}}_{\text{tine}}\,\mathbf{a})_i = L^{\text{fiber}}_{\text{tine}\,ij} a_j$, $(\mathbf{L}_t \mathbf{L}^{\text{fiber}}_{\text{tine}})_{ij} = L_{ik} L^{\text{fiber}}_{\text{tine}\,kj}$, and $(\mathbb{I}\,\mathbf{L}_t)_{ij} = \mathbb{I}_{ijkl} L_{kl}$. The superscripts -1 and t denote respectively the inverse and the transpose of a second- or a fourth-order tensor, e.g., $(\mathbf{L}_t^{t})_{ij} = L_{ji}$ and $(\mathbb{I}^{t})_{ijkl} = \mathbb{I}_{klij}$. The prefixes tr and det indicate the trace and the determinant, the superscript d the deviatoric part, and the subscripts s and a the symmetric and anti-symmetric parts of a second-order tensor. A superimposed dot on a tensor denotes the material time derivative of that tensor. The second-order identity tensor is denoted by $\mathbf{I}$ and its components by δ_{ij}.

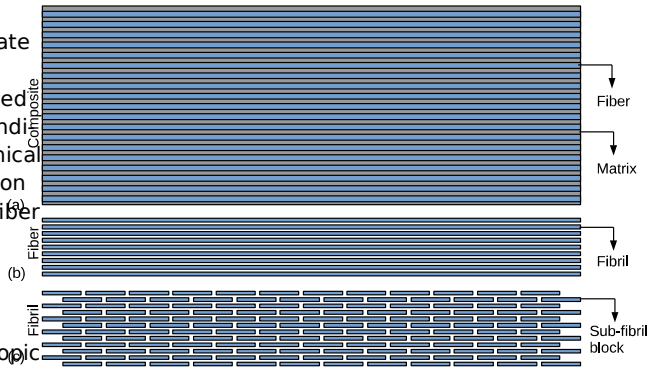

Fig. 2. A simplified schematic representation of the multi-scale microstructure in tendons. Part (a) shows a unidirectional, fiber-reinforced composite, idealizing the actual microstructure in tendons at the higher level. A typical fiber in part (a) is made up of a bundle of aligned long fibrils, as shown in part (b), while each individual fibril consists of a large number of aligned short sub-fibril building blocks, as shown in part (c).

2. Modeling fiber plasticity in soft composites

In this work, we focus our attention on a class of composite materials consisting of a soft matrix reinforced by a single family of fibers, as shown in the schematic representation of Fig. 2(a). The fibers are taken to be aligned along a given direction, defined by the unit vector $\mathbf{n}_0$ in the unstressed state, and to exhibit elastoplastic, transversely isotropic behavior, with symmetry axis $\mathbf{n}_0$. The matrix, on the other hand, is assumed to exhibit isotropic and hyperelastic behavior with respect to the unstressed state.

The above hypotheses are motivated by the microstructure and the local material behavior in tendons. In particular, the proteoglycans and elastin matrix in these materials are amorphous and can accommodate large elastic deformations. In contrast, the collagen fibers are characterized by a preferred direction and exhibit microstructure at two well-separated levels of hierarchy: at the higher level, each individual fiber is actually a bundle of aligned long fibrils (Fig. 2(b)), while at the lower level, each fibril is an assembly of aligned short sub-fibril building blocks (Fig. 2(c)). Under appropriate loading conditions, the sub-fibril blocks can slide with respect to each other along the axis $\mathbf{n}_0$, thus producing a permanent axial strain at the fibril level. The central hypothesis of the present work is that the plastic deformations in the fiber phase play a key role in the loss of ellipticity of the governing equations of equilibrium for the macroscopic behavior of the composite under cyclic loading and, possibly, in the onset of macroscopic instabilities that are observed experimentally in tendons (Fig. 1).

In the sequel of this section, following Pereda et al. (1993), we discuss a transversely isotropic constitutive model, accounting for finite elastic and plastic strains, which is being used in subsequent sections to characterize the material behavior of the fiber phase in the soft composites of interest.

2.1. Kinematics

Consider a homogeneous solid with a reference configuration $\mathcal{B}_0$ at some fixed time t_0 and a current configuration $\mathcal{B}$ at an arbitrary, subsequent time t. Let the deformation of the material from $\mathcal{B}_0$ to $\mathcal{B}$ be described by a one to one and differentiable mapping $\mathbf{x} = \boldsymbol{\chi}(\mathbf{X}, t)$, where $\mathbf{X}$ and $\mathbf{x}$ denote the position vectors of a typical material point in $\mathcal{B}_0$ and $\mathcal{B}$, respectively. The deformation gradient $\mathbf{F}$ is defined as the second-order tensor with components $F_{ij} = \partial \chi_i / \partial X_j$. In order to ensure the impenetrability of the material, it is assumed that $J \equiv \det \mathbf{F} > 0$.

Following Lee (1969), it is further assumed that $\mathbf{F}$ may be decomposed multiplicatively as

$$\mathbf{F} = \mathbf{F}^{e}\mathbf{F}^{p}, \tag{1}$$

where the tensors $\mathbf{F}^e$ and $\mathbf{F}^p$ describe respectively the elastic and plastic parts of the deformation and are, thus, taken to be invertible, with $J^e \equiv \det \mathbf{F}^e > 0$ and $J^p \equiv \det \mathbf{F}^p > 0$.

The decomposition (1) introduces a local intermediate configuration $\mathcal{B}_i$, which may be regarded either as the deformed state for the plastic part or as the reference state for the elastic part of the deformation. The symmetries and constitutive equations for both the elastic and the plastic behavior of the material may be conveniently stated in $\mathcal{B}_i$, as detailed further below. Note, however, that expression (1) defines the intermediate state only up to a rigid body rotation. In order to resolve this ambiguity, in this work, we choose the intermediate configuration to be isoclinic (Mandel, 1971), such that the orientation of the symmetry axis of the material in $\mathcal{B}_i$ remains fixed at all times and, therefore, coincides with its orientation in $\mathcal{B}_0$.

Given the decomposition (1), any elastic and plastic strain measure may be defined in terms of $\mathbf{F}^e$ and $\mathbf{F}^p$, respectively. In this work, we will only make use of the Green elastic strain tensor

$$\mathbf{E}^e = \frac{1}{2}(\mathbf{C}^e - \mathbf{I}), \tag{2}$$

where $\mathbf{C}^e = \mathbf{F}^{e\mathsf{T}}\mathbf{F}^e$ is the elastic right Cauchy–Green deformation tensor and $\mathbf{I}$ is the second-order identity tensor.

Letting $\mathbf{v} = \hat{\mathbf{v}}(\mathbf{x}, t)$ denote the velocity field, velocity gradient $\mathbf{l}$ in $\mathcal{B}$ is defined as the second-order tensor with components $l_{ij} = \partial \hat{v}_i / \partial x_j$. It follows that $\mathbf{l} = \dot{\mathbf{F}}\mathbf{F}^{-1}$, which, by taking into account (1), implies that

$$\mathbf{l} = \dot{\mathbf{F}}^e\mathbf{F}^{e-1} + \mathbf{F}^e\mathbf{l}_i^p\mathbf{F}^{e-1}, \qquad \mathbf{l}_i^p = \dot{\mathbf{F}}^p\mathbf{F}^{p-1}, \tag{3}$$

where $\mathbf{l}_i^p$ is the velocity gradient tensor in the intermediate configuration. The tensors $\mathbf{l}$ and $\mathbf{l}_i^p$ may be decomposed into the deformation rate tensors

$$\begin{aligned} \mathbf{d} &= \mathbf{l}_{\mathrm{sym}} \equiv \mathbf{d}^e + \mathbf{d}^p, & \mathbf{d}^e &= \mathbf{F}^e\left(\mathbf{F}^{e-1}\dot{\mathbf{F}}^{e-1}\right)_{\mathrm{sym}}\mathbf{F}^{e-1}, \\ \mathbf{d}^p &= \mathbf{F}^e\left(\mathbf{l}_i^p\right)_{\mathrm{sym}}\mathbf{F}^{e-1}, & \mathbf{d}_i^p &= \left(\mathbf{l}_i^p\right)_{\mathrm{sym}}, \end{aligned} \tag{4}$$

and the spin tensors

$$\begin{aligned} \mathbf{w} &= \mathbf{l}_{\mathrm{skw}} \equiv \mathbf{w}^e + \mathbf{w}^p, & \mathbf{w}^e &= \mathbf{F}^e\left(\mathbf{F}^{e-1}\dot{\mathbf{F}}^{e-1}\right)_{\mathrm{skw}}\mathbf{F}^{e-1}, \\ \mathbf{w}^p &= \mathbf{F}^e\left(\mathbf{l}_i^p\right)_{\mathrm{skw}}\mathbf{F}^{e-1}, & \mathbf{w}_i^p &= \left(\mathbf{l}_i^p\right)_{\mathrm{skw}}, \end{aligned} \tag{5}$$

where the subscripts ''s'' and ''a'' indicate respectively the symmetric and anti-symmetric part of the second-order tensor to which they are attached.

2.2. Stress power

It follows from the above definitions that the stress power $\mathcal{P}$ per unit volume of intermediate configuration may be decomposed according to into an elastic part $\mathcal{P}^e$ and a plastic part $\mathcal{P}^p$ as follows

$$\mathcal{P} = \boldsymbol{\sigma} \cdot \mathbf{l} = \mathcal{P}^e + \mathcal{P}^p, \qquad \mathcal{P}^e = \mathbf{T}_t \cdot \dot{\mathbf{E}}^e, \qquad \mathcal{P}^p = \mathbf{M} \cdot \mathbf{l}_i^p, \tag{6}$$

where we have introduced the stress measures

$$\boldsymbol{\sigma} = \mathbf{T}_t\mathbf{F}^{e\mathsf{T}}, \qquad \mathbf{T}_t = \mathbf{F}^{e-1}\boldsymbol{\sigma}\mathbf{F}^{e-\mathsf{T}}, \qquad \mathbf{M} = \mathbf{F}^{e\mathsf{T}}\boldsymbol{\sigma}\mathbf{F}^{e-\mathsf{T}}, \tag{7}$$

with $\boldsymbol{\sigma}$ denoting the Cauchy stress tensor. The tensors $\mathbf{T}_t$, and $\mathbf{M}$ in (6) are commonly referred to as the (elastic) Kirchhoff, second Piola–Kirchhoff, and the Mandel stress, respectively. The Cauchy stress $\boldsymbol{\sigma}$ is assumed to be symmetric, so that the tensors $\boldsymbol{\sigma}$ and $\mathbf{T}_t$ are also symmetric, but $\mathbf{M}$ is not symmetric, in general.

Next, we define the elastic and plastic parts of the material behavior in the intermediate configuration. In particular, we first establish appropriate relations between the conjugate variables $(\mathbf{E}^e, \mathbf{T}_t)$ and $(\mathbf{M}, \mathbf{l}_i^p)$, and then we combine these relations to obtain the corresponding rate form of the elastoplastic equations.

2.3. Elastic behavior

The elastic properties of the material are defined in the isoclinic configuration in terms of a strain–energy density function $\psi = \hat{\psi}(\mathbf{E}^e) = \bar{\psi}(\mathbf{C}^e)$, which is such that $\mathbf{T}_t = \psi$ and, therefore,

$$\mathbf{T}_t = \frac{\partial \psi}{\partial \mathbf{E}^e}. \tag{8}$$

For later reference, it is remarked that the rate form of the above constitutive equation is

$$\dot{\mathbf{T}}_t = \mathbb{L}\dot{\mathbf{E}}^e, \qquad \mathbb{L} = \frac{\partial^2 \psi}{\partial \mathbf{E}^e \partial \mathbf{E}^e}. \tag{9}$$

In addition, making use of (7)$_2$ and (9), it is straightforward to show that

$$\begin{aligned} \overset{\circ}{\boldsymbol{\sigma}} &= \mathbb{L}^{\circ}\mathbf{d}, \qquad \mathbb{L}^{\circ}_{3456} = \mathbb{L}_{3961}\mathbf{F}^e_{4I}\mathbf{F}^e_{5J}\mathbf{F}^e_{6K}\mathbf{F}^e_{LI} \\ &+ \frac{1}{2}\boldsymbol{\sigma}_{35}\delta_{46} + \delta_{36}\boldsymbol{\sigma}_{45} + \delta_{35}\boldsymbol{\sigma}_{46} + \delta_{36}\boldsymbol{\sigma}_{45}, \end{aligned} \tag{10}$$

where we have introduced the co-rotational rate $\overset{\circ}{\boldsymbol{\sigma}} = \dot{\boldsymbol{\sigma}} + \boldsymbol{\sigma}\mathbf{w} - \mathbf{w}\boldsymbol{\sigma}$. Note that, the fourth-order modulus tensors $\mathbb{L}^{\circ}$ and $\mathbb{L}$ in (10) and (9) possess both the major and the minor symmetries.

For the purpose of this work, the strain–energy density function $\hat{\psi}$ is assumed to be a transversely isotropic invariant, with the symmetry axis $\mathbf{e}_0$. Hence, the function ψ may be written in the form (Ericksen and Rivlin, 1954; Spencer, 1984)

$$\psi = \hat{\psi}(\mathbf{E}^e) = \bar{\psi}(\iota_1, \iota_2, \iota_3, \iota_4, \iota_5), \tag{11}$$

where ι_1, ι_2, ι_3, ι_4, and ι_5 constitute a complete set of transversely isotropic invariants of $\mathbf{E}^e$, defined by

$$\begin{aligned} &\iota_1 = \mathrm{tr}\,\mathbf{E}^e, \qquad \iota_2 = \frac{1}{2}\left[(\mathrm{tr}\,\mathbf{E}^e)^2 - \mathrm{tr}(\mathbf{E}^e)^2\right], \\ &\iota_3 = \det \mathbf{E}^e \qquad \iota_4 = \mathbf{e}_0 \cdot \mathbf{E}^e\mathbf{e}_0, \qquad \iota_5 = \mathbf{e}_0 \cdot (\mathbf{E}^e)^2\mathbf{e}_0, \end{aligned} \tag{12}$$

with $(\mathbf{E}^e)^2 = \mathbf{E}^e\mathbf{E}^e$. Note that, the functions ι_1, ι_2, and ι_3 are the principal, isotropic invariants of $\mathbf{E}^e$, while ι_4 and ι_5 depend explicitly on $\mathbf{e}_0$. Therefore, in the special case that $\bar{\psi}$ is independent of ι_4 and ι_5, (11) reduces to

$$\psi = \hat{\psi}(\mathbf{E}^e) = \bar{\psi}(\iota_1, \iota_2, \iota_3), \tag{13}$$

and describes an isotropic hyperelastic material. In passing, it is remarked that the properties of the matrix phase in the composite materials of interest are completely characterized by means of a strain–energy function of the form (13).

2.4. Plastic behavior

Motivated by the behavior of collagen fibers in tendon (see Fig. 2 and relevant discussion), we assume that the plastic deformation of the material is constrained to be isochoric and axisymmetric, with the associated symmetry axis being $\mathbf{e}_0$. In particular, we assume that the material obeys the yield criterion

$$\phi(\mathbf{M}, \alpha) = \sigma_n - \sigma_Y(\alpha) = 0, \qquad \sigma_n = \mathbf{e}_0 \cdot \mathbf{M}^s\mathbf{e}_0, \tag{14}$$

along with the associative flow rule

$$\mathbf{d}_i^p = \dot{\lambda}\frac{\partial \phi}{\partial \mathbf{M}}, \qquad \frac{\partial \phi}{\partial \mathbf{M}} = \frac{\partial \sigma_n}{\partial \mathbf{M}} = (\mathbf{e}_0 \otimes \mathbf{e}_0)^s, \tag{15}$$

where $\dot{\lambda} \geq 0$ is the plastic multiplier, to be determined further below, and the superscript ''s'' in the above expressions denotes the deviatoric part of the tensor to which it is attached. The yield stress σ_Y in (14) is assumed to be given as a function of the accumulated plastic strain α, which is also determined further below.

Given that $\mathbf{e}_0$ defines the direction of certain material line elements—which, in the case of tendon, correspond to the fibrils and sub-fibrils—it follows that, in the intermediate configuration,

$$\dot{\mathbf{e}}_0 = \mathbf{l}_i^p\mathbf{e}_0 + \mathbf{e}_0 \otimes \mathbf{e}_0\mathbf{l}_i^p\mathbf{e}_0 - \mathbf{e}_0 \otimes \mathbf{e}_0\mathbf{l}_i^p\mathbf{e}_0 = \mathbf{w}_i^p\mathbf{e}_0 = \mathbf{0}, \tag{16}$$

where $(16)_2$ follows from the flow rule (15), while $(16)_3$ is due to the fact that the intermediate configuration is isoclinic and, therefore, $\mathbf{C}_0 = \mathbf{I}$. Eq. $(16)_3$ implies that $\mathbf{a}_0$ is the axial vector of $\mathbf{L}^p_3$, which in turn allows us to choose

$$\mathbf{a}_0 = \mathbf{e}_3, \tag{17}$$

with no loss of generality (see, e.g., Aravas (1994)).

Thus, we find that $\mathbf{L}^p_3 = \mathbf{e}_3 \otimes \mathbf{e}_3$ and, therefore, $\mathbf{F}^p = \mathbf{F}^{p-1} = \mathbf{e}_3 \otimes \mathbf{e}_3$. Taking into account the flow rule (15), the latter equation implies that $\mathbf{F}^p$ describes an axisymmetric shear of the form

$$\mathbf{F}^p = \mathrm{L}^p_t \mathbf{e}_0 \otimes \mathbf{e}_0 + \mathrm{L}^{p-1/2}_t \mathbf{e}_0 \otimes \mathbf{e}_0 + \mathbf{f}_0 \otimes \mathbf{f}_0, \tag{18}$$

where $\mathbf{e}_0$ and $\mathbf{f}_0$ are any pair of unit vectors in the transverse plane which together with $\mathbf{e}_0$ form an orthonormal basis, while L^p_t is the plastic stretch along $\mathbf{e}_0$, which is given in terms of J^p by

$$\frac{\mathrm{L}^p_t}{\mathrm{L}^p_t} = \frac{2}{3}\mathrm{J}^p \tag{19}$$

In addition, assuming that $\mathbf{T}^p$ is plastic-work conjugate to the axisymmetric stress $\mathbf{T}_n$, so that

$$\mathbf{T}^p = \mathbf{T} \cdot \mathbf{L}^p_3 = \mathbf{T} \cdot \mathbf{e}_3 \otimes \mathbf{e}_3 = \mathbf{t}_n \otimes \mathbf{e}_3 \tag{20}$$

it follows that

$$\mathbf{t}_n = \mathbf{T}^p \mathbf{e}_3 \tag{21}$$

The above expression constitutes the evolution equation for $\mathbf{t}_n$.

Given (15) and (17), the plastic deformation rate and spin tensors $(4)_3$ and $(5)_3$ in the current configuration take the form

$$\mathbf{d}^p = \mathbf{R}\,\mathbf{L}^p_3\,\mathbf{R}^{-1} = \dot{\mathrm{L}}^p_t \mathbf{R}\mathbf{e}_3 \otimes \mathbf{R}\mathbf{e}_3, \tag{22}$$

and

$$\mathbf{w}^p = \mathbf{R}\,\mathbf{L}^p_3\,\mathbf{R}^{-1} = \dot{\mathrm{L}}^p_t \mathbf{n} \otimes \mathbf{R}\mathbf{e}_3, \tag{23}$$

respectively.

Given the yield condition (14) and the evolution equation (21), the consistency condition $\dot{\mathrm{f}} = 0$ takes the form

$$\mathbf{n} \cdot \dot{\mathbf{T}} - \dot{\mathrm{L}}^p_t h = 0, \qquad h = \frac{\partial \mathrm{f}}{\partial \mathrm{L}^p_t}. \tag{24}$$

Taking the time derivative of (7), and making use of the result (10), it is found that

$$\dot{\mathbf{T}} = \mathbb{L}^{ep} : \mathbf{d} - \dot{\mathrm{L}}^p_t \mathbf{m}, \tag{25}$$

where

$$\mathbf{m}_{3456} = \frac{1}{2}\left(\mathbf{I}_{35}\mathbf{n}_{46} - \mathbf{I}_{36}\mathbf{n}_{45} + \mathbf{n}_{35}\mathbf{I}_{46} + \mathbf{n}_{36}\mathbf{I}_{45}\right). \tag{26}$$

Note that the tensor $\mathbf{m}_{3456}$ is anti-symmetric with respect to its first and symmetric with respect to its second pair of indexes. Substituting expression (25) in the consistency condition (24), and making use of the fact that $\mathbf{d} = \mathbf{d}^e - \mathbf{d}^p$, with $\mathbf{d}^p$ given by (22), it can be shown that

$$\dot{\mathrm{L}}^p_t = \frac{1}{\mathrm{H}} \mathbf{n} \cdot \mathbf{d}, \tag{27}$$

where

$$\mathrm{H} = \mathbf{n} \cdot \mathbb{L}^{ep} : \mathbf{R}\mathbf{e}_3 \otimes \mathbf{R}\mathbf{e}_3, \qquad \mathbb{L}^{ep} = 2\mathrm{J}^{-1}\mathbf{F}\frac{\partial \mathrm{L}^p_t}{\partial \mathbf{C}}\mathbf{F}^T + h, \tag{28}$$

where we recall that $(\mathbf{I}\otimes\mathbf{I})_{3456} = \mathbf{I}_{3634}$. It follows from the aforementioned symmetries of $\mathbf{n}$ and $\mathbf{m}$ that the second-order tensor $\mathbf{H}$ is symmetric.

2.5. Incremental elastoplastic behavior

Taking into account the fact that $\mathbf{T}^\nabla = \dot{\mathbf{T}} - \mathbf{w}\mathbf{T} + \mathbf{T}\mathbf{w}$, as well as Eqs. (22) and (23) for $\mathbf{d}^p$ and $\mathbf{w}^p$, respectively, with $\dot{\mathrm{L}}^p_t$ given by (27), the rate Eq. (10) may be recast in the form

$$\mathbf{T}^\nabla = \mathbb{L}^{ep}_{\mathrm{tan}} : \mathbf{d}, \qquad \mathbb{L}^{ep}_{\mathrm{tan}} = \mathbb{L}^{ep} - \frac{\dot{\mathrm{U}}(\mathrm{f})}{\mathrm{H}}\mathbf{R}\mathbf{e}_3 \otimes \mathbf{R}\mathbf{e}_3, \tag{29}$$

where $\mathbf{T}^\nabla = \dot{\mathbf{T}} - \mathbf{w}\mathbf{T} + \mathbf{T}\mathbf{w}$ is the Jaumann derivative of $\mathbf{T}$, and $\dot{\mathrm{U}}(\mathrm{f})$ is the unit step function; recall that $\dot{\mathrm{U}}(\mathrm{f}) = 1$ if $\dot{\mathrm{f}} > 0$ and $\dot{\mathrm{U}}(\mathrm{f}) = 0$ otherwise. Note that the modulus tensor $\mathbb{L}^{ep}_{\mathrm{tan}}$ in $(29)_2$ has both the major and the minor symmetries.

Finally, for the numerical integration of the elastoplastic constitutive equations presented in this section, we refer to the work by Pereda et al. (1993), where an efficient algorithm can be found for a more general class of anisotropic materials which can be easily adapted to the present case.

3. Estimates of the Voigt type for soft composites with fiber plasticity

In this section, we propose a simple constitutive model for the macroscopic behavior of the unidirectional soft composites of interest. The proposed model aims to resolve some basic characteristics of tendon from a micromechanical perspective, such as the ductile response of collagen fibers and the elastic response of the surrounding matrix, but purposely neglects some other well-established features of the response which result from undulation of the collagen fibers at their un-recruited states, such as the toe and linear regimes present in the stress–strain response (Szczesny et al., 2012) and the tension–compression asymmetry. The main motivation for these idealizations is twofold: (i) when plastic deformations are taken into account in macroscopic tendon and connective tissue studies, plasticity is usually lumped at the composite level and the intricate response due to the elastic mismatch between fibers and matrix is neglected, and (ii) focusing on a very simple microstructure will allow us to gain insight on the existence of governing mechanisms that could also dictate the response of more realistic microstructures.

3.1. Effective behavior

Consider a composite material made out of an isotropic and hyperelastic matrix phase, reinforced by a large number of elastoplastic and transversely isotropic fibers, as defined in the previous section. In the undeformed configuration, the fibers are assumed to be aligned along the symmetry axis $\mathbf{e}_0$ of their transverse isotropy. In what follows, we make use of the superscripts ''m'' and ''f'' to distinguish between quantities that refer to the matrix and the fibers, respectively. For instance, the notations v^m and v^f are used for the volume fractions of the phases in the reference configuration, which are such that $\mathrm{v}^m + \mathrm{v}^f = 1$.

In order to determine the macroscopic constitutive behavior of the composite, we employ the approximation of the Voigt type that the deformation gradient field in the composite is uniform all the time. Therefore,

$$\mathbf{F}^m = \mathbf{F}, \qquad \mathbf{F}^f = \mathbf{F} = \mathbf{F}^p\mathbf{F}^p, \tag{30}$$

where $\mathbf{F}$ denotes the macroscopic deformation gradient, while $\mathbf{F}^m$ and $\mathbf{F}^f$ stand for the deformation gradients in the matrix and the fiber phase, respectively. This assumption implies that the corresponding stress field in the composite is uniform per phase and, therefore, the macroscopic Kirchhoff stress $\mathbf{T}$ is given by

$$\mathbf{T} = \mathrm{v}^m\mathbf{T}^m + \mathrm{v}^f\mathbf{T}^f, \tag{31}$$

where $\mathbf{T}^m$ and $\mathbf{T}^f$ are the Kirchhoff stresses in the phases, which are related to the corresponding Cauchy stresses $\boldsymbol{\sigma}^m$ and $\boldsymbol{\sigma}^f$ by

$$\mathbf{T}^m = \mathrm{J}^m\boldsymbol{\sigma}^m, \qquad \mathbf{T}^f = \mathrm{J}^f\boldsymbol{\sigma}^f, \tag{32}$$

where $\mathrm{J}^\alpha = \det\mathbf{F}^\alpha$. Note that, in the context of $(32)_2$, use has been made of the fact that $\mathrm{J}^f = \mathrm{J}^p$, with $\mathrm{J}^p = \det\mathbf{F}^p$, which follows from the plastic incompressibility of the fiber phase. The macroscopic Cauchy stress $\boldsymbol{\sigma}$ can be shown (Hill, 1972) to be given in terms of J and $\mathbf{T}$ by

$$\boldsymbol{\sigma} = \mathrm{J}^{-1}\mathbf{T}. \tag{33}$$

The above result, which holds independently of the Voigt assumption, may be shown directly in the present context by making use of Eqs. (31) and (32), along with the equation $\boldsymbol{\sigma} = \mathbf{W}\boldsymbol{\sigma}$. In connection with the latter equation, it is remarked that, due to the Voigt approximation, the volume fractions of the phases are independent of the applied deformation gradient $\mathbf{F}$.

At this point, it is relevant to recall from the discussion in the previous section that

$$\mathbf{L}_t = \dot{\mathbf{F}}\mathbf{F}^{-1}, \qquad \mathbf{L}_t^{(\alpha)} = \frac{\partial \mathbf{v}^{(\alpha)}}{\partial \mathbf{x}}, \tag{34}$$

where $\mathbf{E}$ is the Green elastic strain tensor given by (2), while $\psi^{(\alpha)} = \psi^{(\alpha)}(\mathbf{E})$ is the strain–energy density of the fiber phase, which is taken to be some given transversely isotropic function of the form (11). For completeness, we also remark that

$$\mathbf{L}_t = \dot{\mathbf{F}}\mathbf{F}^{-1}, \qquad \mathbf{L}_t^{(m)} = \frac{\partial \mathbf{v}^{(m)}}{\partial \mathbf{x}}, \tag{35}$$

where $\mathbf{E}$ is the Green strain tensor in the purely elastic matrix and $\psi^{(m)} = \psi^{(m)}(\mathbf{E})$ is the corresponding strain–energy density, which is assumed to be a given isotropic function of the form (13).

Given that, by assumption, (30) holds at all times, it follows that

$$\mathbf{D}^{(m)} = \mathbf{D}, \qquad \mathbf{D}^{(f)} = \mathbf{D}, \tag{36}$$

where $\mathbf{D}$ is the macroscopic velocity gradient, while $\mathbf{D}^{(m)}$ and $\mathbf{D}^{(f)}$ are the velocity gradients in the phases. Hence, the Jaumann derivatives (i.e., the co-rotational rates with the macroscopic spin $\boldsymbol{\Omega} = \mathbf{W}$) of $\boldsymbol{\tau}$ and $\boldsymbol{\sigma}$ are given by

$$\overset{\nabla}{\boldsymbol{\tau}}{}^{(f)} = \mathbb{L}^{(f)}\mathbf{D}, \qquad \overset{\nabla}{\boldsymbol{\tau}}{}^{(m)} = \mathbb{L}^{(m)}\mathbf{D}, \tag{37}$$

where $\mathbf{D} = (\mathbf{L} + \mathbf{L}^{T})/2$ is the macroscopic deformation rate tensor, whereas $\mathbb{L}^{(f)}$ and $\mathbb{L}^{(m)}$ are the corresponding incremental modulus tensors of the phases. Recall that the components of $\mathbb{L}^{(m)}$ are determined by expression (29)$_2$ in the previous section. In addition, it follows from the result (10)$_2$ that the components of $\mathbb{L}^{(m)}$ are given by

$$\mathcal{L}^{(m)}_{3456} = \lambda_m \delta_{34}\delta_{56} + \mu_m\left(\delta_{35}\delta_{46} + \delta_{36}\delta_{45}\right) + \frac{1}{2}\left(\mathcal{C}^{(m)}_{35}\delta_{46} + \delta_{36}\mathcal{C}^{(m)}_{45} + \mathcal{C}^{(m)}_{35}\delta_{46} + \delta_{36}\mathcal{C}^{(m)}_{45}\right),$$
$$\mathcal{C}^{(m)}_{9A} = \frac{\partial^2 \psi^{(m)}}{\partial E_{9r}\partial E_{rA}}. \tag{38}$$

Thus, taking into account the expressions (31) and (37), we find that the Jaumann derivative $\overset{\nabla}{\boldsymbol{\tau}}$ of the macroscopic Kirchhoff stress is given by

$$\overset{\nabla}{\boldsymbol{\tau}} = \mathbb{L}\mathbf{D}, \qquad \mathbb{L} = \mathbb{W}\mathbb{L}^{(m)} + \mathbb{W}\mathbb{L}^{(f)}. \tag{39}$$

Note that, the macroscopic modulus tensor in (39), just like its local counterparts $\mathbb{L}^{(m)}$ and $\mathbb{L}^{(f)}$, possesses both the major and the minor symmetries.

4. Incremental equations of equilibrium: local and global loss of ellipticity

The ellipticity of the incremental equations of equilibrium for the homogenized composite of interest and for its homogeneous phases may be concisely analyzed in a unified manner. In particular, in this section we focus our considerations on a homogeneous solid, characterized by an incremental constitutive equation of the form

$$\overset{\nabla}{\boldsymbol{\tau}} = \mathbb{L}\mathbf{D}, \qquad \mathbb{L} = \mathbb{L}^{T} - \boldsymbol{\tau} \otimes \mathbf{I}, \tag{40}$$

where $\overset{\nabla}{\boldsymbol{\tau}}$ is the Jaumann derivative of the Cauchy stress $\boldsymbol{\tau}$. Note that, the macroscopic constitutive equation (39) for the composite may be easily recast in the form (40), with the modulus tensor $\mathbb{L}$ given by (39)$_2$. The corresponding constitutive equation for each of its constituent phases may also be written in the form (40), where $\mathbb{L}$ and $\boldsymbol{\tau} = \boldsymbol{\sigma}$ with $\alpha = f$ for the matrix and $\alpha = 1$ for the fiber phase.

For latter reference, it is remarked that Eq. (40) may be rewritten in the form

$$\dot{\boldsymbol{\sigma}} = (\mathbb{L} - \mathbb{R})\mathbf{D} \qquad \text{or} \qquad \dot{\sigma}_{34} = \mathcal{L}_{3456}\dot{E}_{56} - \mathcal{R}_{3456}\frac{\partial W}{\partial E_{56}}, \tag{41}$$

where $\mathbb{R}$ is a fourth-order tensor with components

$$\mathcal{R}_{3456} = \frac{1}{2}\left(\delta_{35}\sigma_{46} - \delta_{36}\sigma_{45} - \sigma_{35}\delta_{46} + \sigma_{36}\delta_{45}\right). \tag{42}$$

Note that $\mathbb{R}$ is symmetric with respect to its first and antisymmetric with respect to its second pair of indexes.

In the absence of body forces, the equilibrium equations $\partial\sigma_{34}/\partial x_4 = 0$ for the material under consideration may be written in the rate form

$$\frac{\partial \dot{\sigma}_{34}}{\partial x_4} - \frac{\partial \sigma_{34}}{\partial x_5}\frac{\partial \dot{W}}{\partial E_{45}} = 0, \tag{43}$$

which, by making use of (41), specialize to

$$\mathcal{L}_{3456}\frac{\partial^2 \dot{W}}{\partial x_4 \partial x_6} + \left[\frac{\partial}{\partial x_4}\mathcal{L}_{3456} - \mathcal{R}_{3456}\frac{\partial \sigma_{34}}{\partial x_5}\right]\frac{\partial \dot{W}}{\partial x_6} = 0. \tag{44}$$

Expressions (44) constitute a system of linear PDEs of the second-order for the velocity field v_4 in the material.

Adopting standard terminology in the linear theory of PDEs (e.g., Renardy and Rogers (2004)), the term involving the second-order derivatives of v_4 in Eqs. (44) is referred to as the principal part of these equations, while the second-order tensor with components

$$Q_{35} = \mathcal{L}_{3456}n_4 n_6, \tag{45}$$

where n is any non-zero vector, is referred to as the symbol of the principal part. If $\det \mathbf{Q} \neq 0$ for all real $\mathbf{n}$, then the system of PDEs (44) is called elliptic, it has no real characteristic surfaces and admits no solutions with discontinuous partial derivatives.

For the purpose of this work, we henceforth restrict attention to uniform deformation paths, so that the fourth-order tensors $\mathbb{L}$ and $\mathbb{R}$ — which determine the symbol $\mathbf{Q}$ and, in extend, the type of the system of PDEs (44) — are independent of $\mathbf{x}$. It is important to bear in mind, however, that both $\mathbb{L}$ and $\mathbb{R}$ depend inherently on the deformation gradient $\mathbf{F}$, as well as on the current state of the material, as defined by the associated internal variables. With no loss of generality, it is convenient to view a path of deformation as being applied on the initially undeformed material by a uniform deformation gradient $\mathbf{F} = \mathbf{F}(\lambda)$, which varies (monotonically or not) with time from its initial value $\mathbf{F}(0) = \mathbf{I}$.

For any given deformation path, the system of PDEs (44) for the elastoplastic materials of interest is known to be strongly elliptic (i.e., $\det \mathbf{Q} > 0$ for all $\mathbf{n} \neq \mathbf{0}$) in the linear-elastic regime, but as the deformation becomes nonlinear, a critical state may be reached at which the governing equations o equilibrium (44) may lose ellipticity. This happens when there exists at least one real vector $\mathbf{n} \neq \mathbf{0}$ for which

$$\det \mathbf{Q} = 0. \tag{46}$$

When the above condition is first met, it becomes possible to have solutions with discontinuous partial derivatives of v_4 across a characteristic surface with normal n. The emergence of such discontinuous solutions is often regarded as a precursor for the development of material instabilities and failure, such as the formation of shear and kink bands, and it is therefore of great significance. It should be emphasized, however, that the loss of ellipticity (LOE) condition (46) is necessary, but not sufficient for the onset of instabilities. Note that, in order to examine (46) at any given stage of the deformation, it suffices to restrict the analysis to unit vectors $\mathbf{n}$.

In passing, it is remarked that the condition derived by Rice (1976) (see also Rudnicki and Rice, 1975) for the localization of deformation in a narrow band of a homogeneously deformed, homogeneous solid, exhibiting piecewise linear incremental behavior, can be shown to be equivalent to the LOE condition (46).

The onset of the LOE of the governing equilibrium equations is discussed in more detail in the following section, in the context of specific constitutive models and loading conditions, both at the macroscopic level of the composite and at the microscopic level of its constituent phases. As indicated earlier, the failure of ellipticity which is examined in the present work is exclusively induced by the variation of the fourth-order tensors $\mathbb{C}$ and $\mathbb{R}$ with the prescribed deformation. Given that these tensors represent inherent material properties, in what follows, the onset of the LOE of the corresponding equilibrium equations for the material under consideration is simply referred to as the LOE of that material.

5. Results and discussion

In this section, we present the results of mechanical response and LOE for a reinforced material composed by 80% in volume of ductile fibers embedded in an elastic matrix. The matrix is taken to be hyperelastic and its free energy density function follows a compressible neo-Hookean material model

$$\overline{\psi}^{m} = \frac{\overline{\mu}^{m}}{2}(\bar{\imath}_1 - 3 - 2\ln \overline{J}^{m}) + \frac{\overline{\lambda}^{m}}{2}(\overline{J}^{m} - 1)^2, \tag{47}$$

where $\bar{\imath}_1 = \mathrm{tr}\,\bar{\mathbf{C}}$ is the first invariant of $\bar{\mathbf{C}}$ calculated using the total deformation gradient $\bar{\mathbf{F}}$. The fibers are taken to be elastoplastic and its elastic properties are defined in terms of a compressible neo-Hookean model with an additional standard reinforcement term $\psi_4(\bar{\imath}_4^e)$ (Triantafyllidis and Abeyaratne, 1983; Merodio and Ogden, 2002), due to the microstructure of the fiber material, as seen in Fig. 2(b), consisting of aligned fibrils

$$\overline{\psi}^{f} = \frac{\overline{\mu}^{f}_{\mathrm{line}}}{2}(\bar{\imath}_1^e - 3 - 2\ln \overline{J}^{f}) + \frac{\overline{\lambda}^{f}_{\mathrm{line}}}{2}(\overline{J}^{f} - 1)^2 + \frac{\overline{\eta}}{2}(\bar{\imath}_4^e - 1)^2, \tag{48}$$

where $\bar{\imath}_1 = \mathrm{tr}\,\bar{\mathbf{C}}$ and $\bar{\imath}_4 = \mathbf{a}_0 \cdot \bar{\mathbf{C}}\mathbf{a}_0$ are the first and fourth invariants of $\bar{\mathbf{C}}$, respectively, calculated from the elastic part of the deformation gradient $\bar{\mathbf{F}}^e$. For both matrix and fibers, the value of $\overline{\lambda}$ is chosen to be large enough to obtain nearly incompressible phases. In (48), the reinforcement parameter $\overline{\eta} = 0$ retrieves to the original neo-Hookean model, while $\overline{\eta} \to \infty$ corresponds to an inextensible material (Qiu and Pence, 1997b). This reinforcement function has its second derivative given by $\psi_4''(\bar{\imath}_4^e) = \overline{\eta}$, and since we choose values of reinforcement parameter to be $\overline{\eta} \geq 0$, we obtain $\psi_4''(\bar{\imath}_4^e) \geq 0$ and the function $\psi_4(\bar{\imath}_4^e)$ is convex (Tiel, 1984). The neo-Hookean model representing the matrix phase in our formulation is known to have a stable response, however it is also known thermodynamic instability may arise from the reinforcement term in the augmented neo-Hookean model used for the fiber phase (Qiu and Pence, 1997b; Guo et al., 2007). The specific free energy density function of the fiber phase, as prescribed in (48) has to be further examined, as a thermodynamic instability indicated that the material model no longer represents the actual material behavior. We detail the analysis of the thermodynamic limit of energy functions in Appendix A.

The plastic behavior of the fibers follows the rules in Section 2.4, where the yield stress function in (14) is specialized to

$$\sigma_Y = h_0 \bar{\varepsilon}^p + \sigma_0 \left[1 - \exp\left(-\frac{\bar{\varepsilon}^p}{\varepsilon_0}\right)\right]. \tag{49}$$

This hardening model was proposed by Gasser and Holzapfel (2002) and we chose it because we wanted to account for possible nonlinearities in the internal evolution of the variables. In fact, as discussed by Sun and Chen (1989), fiber composites do not show a well-defined yield point and nonlinearity appears in the stress–strain relation gradually, which is a statement valid for a hierarchical fiber material, as seen in Bosia et al. (2010).

The loading is 3D uniaxial stress applied in the initial direction of the fibers $\mathbf{a}_0$, which in our systems coincide with the first basis vector of the Cartesian coordinate system, i.e., $\mathbf{a}_0 \equiv \mathbf{e}_1$. The numerical experiments conducted in this section are displacement controlled, prescribing the principal stretch λ_1 in the direction of the loading, and calculating the other corresponding principal stretches λ_2 and λ_3 according to the uniaxial stress state, i.e., $\bar{s}_{33} = 0$ for $\lambda_3, \lambda_4 \neq 1, 1$.

All elastic moduli and stress normalizations are with respect to the shear modulus of the fibers, $\overline{\mu}^{f}_{\mathrm{line}}$. The normalized bulk and shear moduli for the fibers and matrix are taken to be $\overline{\lambda}^{f}_{\mathrm{line}} = \overline{\lambda}^{m} = 1000$ and $\overline{\mu}^{f}_{\mathrm{line}} = 1$, $\overline{\mu}^{m} = 10$, respectively. The overlines that denote normalization are hereon omitted, thus all stresses and moduli that appear are normalized. For the plastic response of the fibers, we use a normalized yield stress of $\sigma_Y = 1500$.

First, we investigate the material response of the composite, as well as the material response in each phase through one loading/unloading cycle. For this, we consider the cases of a perfectly plastic response and a hardening response for the fiber phase. Following, we investigate the implications of thermodynamic stability of the material model studied in this work. In the final part of this section, we investigate the material stability of the composite under several loading/unloading cycles, where we focus on the LOE in the composite as well as LOE of the material in the fiber phase. We performed this last analysis on materials with different normalized fiber reinforcement moduli ($\overline{\eta} = 10, 1000$), with and without hardening in order to analyze the influence of fiber stiffness and plasticity in the overall material response and stability. The parameters of the hardening model used are $h_0 = 50$, $\sigma_0 = 200$ and $\varepsilon_0 = 0.1$.

5.1. General response and thermodynamic limit

We first perform a single loading/unloading cycle in tension, starting from the unstretched state where $\bar{\mathbf{F}} = \mathbf{I}$, reaching a maximum stretch of $\lambda_{t1} = 2.5$ in the loading direction and returning to a state where the stretch in the loading direction is $\lambda_1 = 1$. Fig. 3 outlines the relationship between the Kirchhoff stress in the direction of the loading ($\bar{s}_{11}$), for the composite (Fig. 3(a)), the fibers (Fig. 3(b)) and the matrix (Fig. 3(c)), plotted against the stretch λ_1. As seen in Fig. 3(b), the fibers reach the yield point and present an elastoplastic behavior beyond that point, whereas the response of the matrix is purely elastic (Fig. 3(c)). The response with and without hardening can be identified between the solid and the dashed lines in Fig. 3.

As previously mentioned, the material model used to represent the fibers following the elastic strain–energy density in (48) can present a thermodynamic instability when subjected to uniaxial compressive stress. Beyond the onset of this instability, the material model no longer represents the physical behavior of the material and thus cannot be used. Thus we wish to study this pathology of the model for the specific material parameters that we use in this paper. From (A.2), it follows that the material is stable as long as the second derivative of the strain–energy function remains greater or equal to zero. The second derivative of the strain–energy function denotes the slope of the stress–stretch relationship. For this investigation, we restrict our attention to the elastic response prior to yielding. To perform this task, we consider a body composed of just the fiber material experiencing a homogeneous stress state under uniaxial loading, and we test a range in tension and compression without the consideration of plasticity. It is important to note that the thermodynamic instability is present even for the purely elastic case. In Fig. 4(a), the elastic stress–stretch response of the fibers is calculated in uniaxial loading, under tension and compression, for different values of the anisotropic reinforcement modulus $\overline{\eta}$. When loaded in compression (for an increasing compressive load, starting from $\lambda_1 = 1$), the response shows a change in the sign of the slope of the stress–stretch curve, which indicates a violation of the thermodynamic stability, rendering the results beyond this point as non-physical. In fact, to reach an extreme compression state, i.e., $\lambda_1 = 0$, we would expect to impose a high level of compressive stress, i.e., $\bar{s}_{11} \to -\infty$; an observation not consistent with the results of the model. As seen in Fig. 4(b), the higher the anisotropic reinforcement modulus, the earlier the thermodynamic instability occurs. As we approach $\overline{\eta} = \infty$, a

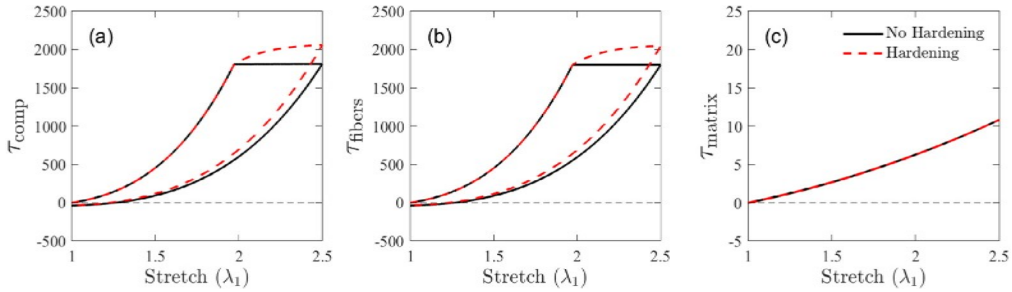

Fig. 3. General stress–stretch response of the material (stretch in the direction of the fibers λ_{fb} spatial Kirchhoff stress in the direction of loading) in which the black line represents the curve for a material with no evolution of internal variables and red lines represents a material subjected hardening effect for (a) composite (b) only the stress on fibers phase (c) only the stress on the matrix phase.

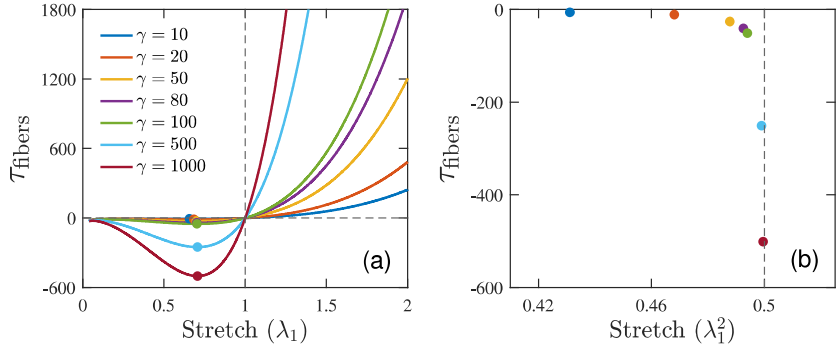

Fig. 4. Limit up to which the material model is stable and can be used to represent the material constitutive behavior for different values of reinforcement modulus. (a) shows the elastic stress–stretch curves for fibers loaded uniaxially, instability occurs for compressive stretches and starts where the circles are plotted. (b) shows the compressive stress and square of stretches in the direction of the fibers at which instability occurs for each stress–stretch curve in (a).

limit of critical stretch is attained with $\lambda_1^2 = 0.5$, where the instability occurs. Summarizing, the pathology of the material model employed for the fiber phase emanated at moderate to high compression during uniaxial loading. As the goal of this study is to study load cycling in tension the material model can still be valid. Moving forward it will be crucial to look at the individual stress–strain response of the fiber phase to make sure thermodynamic stability is maintained in more complex elastoplastic loading/unloading cycles. Nevertheless, in Appendix B we consider a strain–energy function (DeBotton et al., 2006) which does not violate the thermodynamic limit. We investigate the response of the new material model to verify that the trends of LOE are not affected by the use of a constitutive model which is unstable for a known range of deformations.

5.2. Loss of ellipticity during non-monotonic loading

To examine localization during non-monotonic loading, as motivated by the discussion for tendon, we consider a fiber-reinforced composite material under uniaxial loading. The material experiences a homogeneous stress state in each individual phase, following the Voigt assumption. We impose the load by applying a stretch λ_1 starting from the undeformed configuration ($\lambda_1 = 1$) and incrementally increase it to a maximum tensile stretch in that cycle $\lambda_1^{max,i}$, where the superscript $i \in [1, 8]$ is an integer representing the cycle number, where 8 is the total number of cycles (e.g. $\lambda_1^{max,1} = 2.5$ in the first cycle), see Fig. 5(a). From the maximum tensile stretch, we decrease λ_1 by small increments into the compressive stretch regime, down to a minimum stretch value λ_1^{min}. Next, we start a new cycle by increasing the stretch again to a higher value for the maximum stretch ($\lambda_1^{max,i+1} > \lambda_1^{max,i}$) and then compress to attain λ_1^{min}, which does not depend on the cycle number. We repeat this procedure for the total number of cycles. In each of the loading cycles, we check for LOE in the composite, as well as in the fiber phase, using the condition formulated in Section 4.

Through this study we investigate the influence of the reinforcement modulus γ and hardening on the material stability of the composite. We first study the case of a material with reinforcement modulus of $\gamma = 10$ with perfectly plastic fibers. Following, we study two cases with hardening, and reinforcement modulus at two discrete levels, $\gamma = 10$–1000, spanning two orders of magnitude. We conduct this study to investigate the effect of different ratios of reinforcement modulus with respect to the matrix shear modulus.

Material with low reinforcement modulus ($\gamma = 10$) without hardening. For the case of a material with a reinforcement modulus of $\gamma = 10$ without hardening, results are shown in Fig. 5, Fig. 6 and Table 1. We applied 11 loading cycles, that are individually numbered in Fig. 5(a), which shows the evolution of the Kirchhoff stress for the composite versus the stretch in the loading direction. It is important to note that cycle 1 is purely elastic, during tensile loading, tensile unloading, as well as compressive loading and unloading. Cycles 2–11 exhibit an elastic and elastoplastic response during tensile loading, purely elastic response during tensile unloading, and a purely elastic response during compressive loading and unloading. The thermodynamic material stability limit, following the discussion in Section 5.1, will also point to the minimum compressive stretch for which the material description is valid. That means that the compressive response, numerically calculated up to very small values of $\lambda_1 \to 0$ might not be acceptable below a certain stretch threshold $\lambda_1^{ther\,m,cr\,it}$. This threshold has no impact on the rest of the results as compressive loading and unloading are completely elastic, thus there are no history-dependent processes that could be influenced by this pathology. In the numerical calculation, we check for LOE for each increment of the load. We also check for the threshold of the thermodynamic material instability, $\lambda_1^{ther\,m,cr\,it}$, for each cycle by looking at the fiber stress–stretch response.

We first focus on LOE of the composite. To do that, we zoom in on the stress–stretch response. Fig. 5(b) corresponds to a segment of Fig. 5(a) in the compressive regime for the 11 cycles, where following the curves from right to left corresponds to compressive elastic loading.

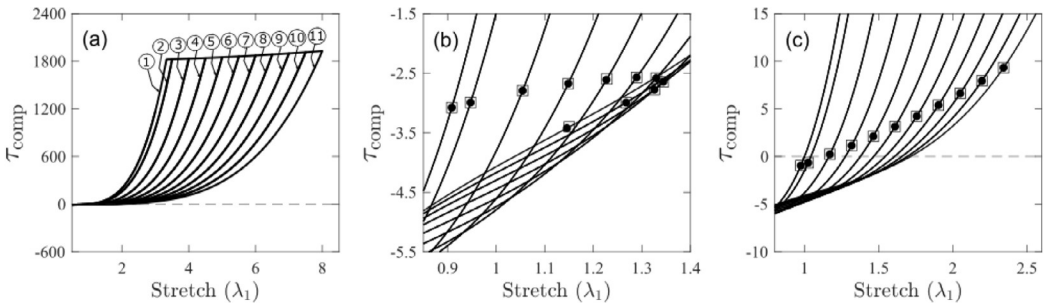

Fig. 5. Stress–stretch curve of the composite and LOE points for a material with reinforcement modulus $\mathcal{E}_r = 10$ and no hardening. (a) shows the 11 loading and unloading steps applied to the material. (b) shows LOE in the composite, where the squares with circles inside represent the points of LOE. (c) shows the critical stretches and composite stress for LOE analysis in the fibers.

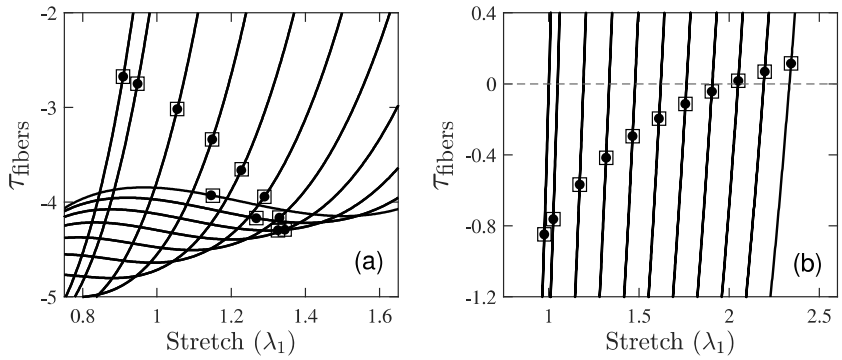

Fig. 6. Stress–stretch curve of the fibers and LOE points for a material with reinforcement modulus $\mathcal{E}_r = 10$ and no hardening. (a) shows the critical stretches and fibers stress for LOE analysis in the composite, where the squares with circles inside represent the points of LOE. (b) shows LOE in the fibers.

The Kirchhoff effective stress for the composite is plotted against the stretch in the loading direction. Squares with circles inside correspond to positions where LOE occurs following the elastoplastic LOE calculation (this convention to represent LOE points is followed for the rest of the paper). We observed that LOE for the composite occurs during compressive loading as seen in Fig. 5(b). The critical stretch, determined by the LOE, occurs at lower absolute stresses and higher stretches for higher cycles, as plasticity is increasingly induced, up to the 7th cycle. For instance, in the first cycle, we observe that the critical stress is $\mathcal{T}^{\text{crit, 1}}_{\text{comp}} \approx -3.1$ and the critical stretch is $\lambda^{\text{crit, 1}}_{1t} \approx 0.9$ while for the 5th cycle, $\mathcal{T}^{\text{crit, 1}}_{\text{comp}} \approx -2.6$ and $\lambda^{\text{crit, 1}}_{1t} \approx 1.29$. However, after the 7th cycle, there is a change to that trend. To rationalize why this occurs, we focus on the stress–stretch response of the fibers in the composite, plotting the Kirchhoff stress for the fiber against the stretch in the loading direction in Fig. 6(a). In this plot it is clearly seen that LOE occurs past the threshold of the thermodynamic material instability, $\lambda^{\text{ther m,crit}}_{1t}$, for cycles 8–11, as the slope sign during compressive loading changes at higher stretches compared to when LOE occurs.

Following, we focus on LOE of the material in the fiber phase as the composite experiences the same loading cycles (Fig. 5(a)). To do that, we zoom in on the stress–stretch response and investigate first Fig. 5(c), which corresponds to a segment of Fig. 5(a) for the 11 cycles. Here, following the curves from right to left also corresponds to unloading or compressive loading steps. The Kirchhoff effective stress for the composite is plotted against the stretch in the loading direction. From that, we observe that LOE in the fibers occurs not only during a macroscopic compressive loading (cycles 1–2) but mostly during elastic unloading in macroscopic tension (cycles 3–11), as seen in Fig. 5(c), which is consistent with the observation of fiber kinking in tendon during cyclic loading. Similar to the onset of instability in the composite, LOE in the fiber phase occurs earlier during the compressive loading or tensile unloading process for higher cycles. As plasticity is induced (from cycle 1 to 11), the critical stresses and stretches increase. To investigate if the LOE prediction for the fibers is valid in each cycle, we look at the stress–stretch response of the fibers in the composite, plotting the fiber Kirchhoff stress against the stretch in the loading direction in Fig. 6(b). In this plot, it is clearly seen that LOE of the fibers never occurs past the threshold of the thermodynamic material instability, $\lambda^{\text{ther m,crit}}_{1t}$, as the slope of the stress–stretch curves changes sign much later during the compressive loading steps, at a stress range that is not shown in this zoomed-in section of the fiber stress–stretch plot. However, we can observe from the segment of the fibers stress–stretch plot in Fig. 6(a) that the change in sign of the slop occurs at stresses lower than any critical stresses on the fiber phase shown in Fig. 6(b), thus the predictions of LOE in the fiber phase in all 11 cycles are acceptable.

The main observation from the LOE calculated in the fiber phase (reported in Fig. 5(c) and Fig. 6(b)), is that instabilities in the fiber phase, for high cycle numbers, can occur at tensile stresses at both the composite and at the fiber level. The critical stress in the composite is compressive in the first, and purely elastic, cycle and in the second cycle; however, from the third to eleventh cycles, characterized by higher levels of plastic deformation, LOE is found when the composite experiences tensile stresses. A similar trend is noted on the critical stresses on the fiber phase in Fig. 6(b), which shows that LOE occurs when the fibers are under compressive stress for the first 8 cycles, but under tensile stress from the 9th cycle onwards. This finding is one of the key results obtained in this study because, from widely accepted literature in reinforced materials, this type of instabilities is known to occur when the material is subjected to compressive loading. In contrast, here we suggest that it can also occur when the material experiences a tensile stress state.

By examining LOE in the composite (Fig. 5(b) or Fig. 6(a)), or in the fiber phase (Fig. 5(c) or Fig. 6(b)), we note that many of the instabilities found occur at tensile stretches ($\lambda^{\text{crit}}_{1t} > 1$). Nevertheless, when we look at the elastic component of the critical stretches of the fibers on Table 1, we notice that the critical elastic stretches of the fibers are compressive ($\lambda^{\text{crit}}_{1e} < 1$) on both composite LOE analysis (first row) and fibers LOE

Table 1
Critical elastic stretches for each unloading step of a composite with reinforcement = 10 and no hardening. The second row shows the critical stretches for the LOE analysis in the composite and the third row shows the critical stretches for the ellipticity analysis in the fibers.

$\lambda^{1}_{t,crit}$	Step										
	1	2	3	4	5	6	7	8	9	10	11
LOE comp	0.9084	0.9013	0.8779	0.8500	0.8173	0.7807	0.7381	0.6888	0.6308	0.5629	0.4769
LOE fibers	0.9750	0.9752	0.9752	0.9752	0.9752	0.9752	0.9752	0.9752	0.9752	0.9752	0.9752

analysis (second row). This contrasting behavior suggests that there is a mismatch in the elastic deformation field of the phases, while the total deformation field remains compatible following the Voigt assumption. This mismatch leads to a bulk stress during unloading: as the elastic strain is released, the composite reaches an intermediate configuration, which is macroscopically stress-free; however, at the same time, each phase (matrix and fibers) experiences a non-zero stress state. For instance, the stress-free configuration of the composite during the 11th cycle, after tensile unloading, occurs at around $\lambda_t \approx 1.7$, (where the last curve cross the $\mathfrak{fb}$-axis in Fig. 5(c)), in contrast, we note from Fig. 6 that at the same load $\lambda_t = 1.7$, the stress on the fibers is negative.

Another interesting remark in this set of results is on the difference between the LOE prediction in the composite and the LOE prediction in the fiber phase. Comparing the LOE in the composite shown in Fig. 5(b) and Fig. 6(a) with LOE in the fiber phase shown in Fig. 5(c) and Fig. 6(b), we observe that instability in the fibers is expected to precede the onset of instability in the composite, if the LOE leads to a bifurcated state. We additionally highlight that LOE occurred for values of angle near $\pi/2$, which corresponds to a configuration where the surface of discontinuity have their normal aligned with the fiber reinforcement. As discussed earlier, this configuration of the surface of discontinuity is expected to the localization pattern of the kink-band type. It is also worth noting that LOE was not observed during plastic loading for any of the test cases.

We finally note that LOE in the fibers can occur in tension due to the fact that, even though the composite is under a uniaxial stress state, the phases are individually experiencing an axisymmetric stress state since they are not fully incompressible. We note that we chose different levels of compressibility for the two phases (different bulk to shear modulus ratios) and this introduces an axisymmetric stress state in the phases, where the stress components $\mathfrak{S}^{1}_{22} = \mathfrak{S}^{1}_{33} \neq 0$ and $\mathfrak{S}_{22} = \mathfrak{S}_{33} \neq 0$. For the fiber phase, when $\mathfrak{S}^{1}_{11} > 0$ and $\mathfrak{S}^{1}_{22} = \mathfrak{S}^{1}_{33} > 0$ the LOE can occur due to the presence of a pressure which does not affect LOE.

Material with low reinforcement modulus (=10) with hardening. We now modify the previous material model with reinforcement parameter = 10 to incorporate hardening effects with an evolution function defined in (49). We impose the same loading conditions of 11 cycles of uniaxial load applied in the direction of the fibers, and observe the stress–stretch response of the composite shown in Fig. 7. In Fig. 7(b), we take a segment of Fig. 7(a) and plot the Kirchhoff stress–stretch curves in addition to the LOE points (squares with circle inside). In Fig. 8(a), we plot the Kirchhoff stress for the fiber against the stretch and, from that, we detect which of those LOE points calculated for the composite are valid. We note that, for the cycles 8–11, LOE occur at points after the change in sign of the stress–stretch curves for those cycles, hence, the only acceptable loss of ellipticity calculations are for cycles 1–7. Next, we study LOE in the fiber phase in Fig. 7(c) and Fig. 8(b). In Fig. 7(c), we show the stress–stretch response of the composite and note that LOE occurs at compressive states only for the first two cycles. In Fig. 8(b), we show the stress–stretch response for the fibers and LOE points, which happen, at all cycles, before the thermodynamic limit, and, at compressive stress for the first 9 cycles and at tensile stresses for the last two. In summary, we conclude that, by adding hardening to the model, the stress–stretch curves and the critical stretches at which LOE occurs, for both the composite and matrix phases, do not change significantly. Examining Table 2, we notice that the elastic critical stretches of the fibers are also compressive.

Material with high reinforcement modulus (=1000) with hardening. The last case of our results consists of a material with an even higher anisotropic reinforcement parameter, = 1000, and with hardening. Fig. 9(a) shows the stress–stretch response for this material subjected to 13 loading cycles imposed in the direction of the fibers. We observe that, by increasing the reinforcement parameter, yielding starts for an even lower stretch value in the first cycle (compare to Fig. 7(a)). In Fig. 9(b), we look at the stress–stretch response of the composite from a segment of Fig. 9(a) and plot the LOE points obtained from the composite instability analysis. LOE in the composite occurs for a compressive stress state for all the cycles and the critical points predicted in this analysis are acceptable since they lie before the thermodynamic limiting stretches $\lambda^{ther\,m,cr\,lim}_{1t}$. The last can be confirmed by looking at Fig. 10(a), which shows the fiber stress–stretch curves and the LOE of composite, which clearly occurs much before the change in sign of the slope of the fiber stress–stretch curve in all 13 cycles. If we focus on the LOE on the fiber phase for this strongly reinforced material, we observe some interesting results. Fig. 9(c) shows the stress of the composite plotted against the stretch, which is also a segment of Fig. 9(a) but in addition of the points of LOE of the fibers. The first and purely elastic cycle is the only cycle where the instability occurs when the composite is in compression. As plastic deformation is induced for the second and later cycles, the composite loses ellipticity under a tensile stress state. Unlike the material with reinforcement parameter of = 10 with hardening, the material with = 1000 has all plastic cycles losing ellipticity in the tensile range of loading. This fact suggests that plasticity, induced by the reinforcement term $(I_4 - 1)$ in the strain–energy function in (48), and therefore enhanced by a higher reinforcement parameter , induces the material to lose ellipticity earlier and at tensile stresses. When we turn our attention to the stress state of the fibers in those points of instability in Fig. 10(b), we see a similar response. The fibers are under compression at the first point of LOE, but under tension for all the other cycles, which are plastic. This response suggests that, as we increase the magnitude of the plastic deformation (by increasing the reinforcement parameter that causes plasticity to happen or by stretching the material further into the yield point), LOE (and possibly the instabilities) in fibers of a composite material tends to occur in a different stress state, from a compressive to a tensile regime. Table 3 includes the critical elastic stretches for each unloading step for the composite and the fiber phase.

As previously mentioned, in Appendix B we use an alternate strain–energy function (DeBotton et al., 2006) for the elastic response of the fiber phase, which does not violate the thermodynamic limit. Thus we are able to test the same loading routine and search for loss of ellipticity in the composite and in the fibers. We focus on the cases where the reinforcement modulus is = 1000, consider hardening effects and keep all the other parameters the same. The trend of the results from Appendix B is in agreement with the trend of results presented in this section, confirming that all the conclusions that were made for our material system can be generalized to composite with an elastic matrix and elastoplastic fibers.

6. Concluding remarks

In this work, we investigate the interplay of an elastic matrix material with ductile fibers of a unidirectionally fiber-reinforced soft composite material to the LOE of the governing equations of equilibrium of the composite subjected to non-monotonic tensile loading

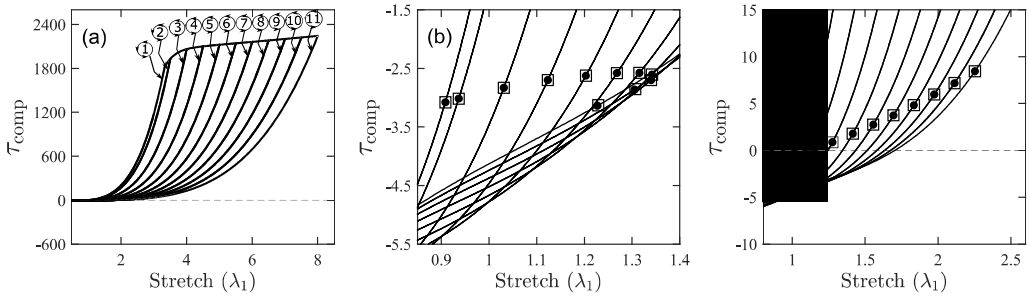

Fig. 7. Stress–stretch curve of the composite and LOE points for a material with reinforcement modulus $\frac{E_f}{E_m} = 10$ with hardening. (a) shows the 11 loading and unloading steps applied to the material, (b) shows LOE in the composite, where the squares with circles inside represent the points of LOE. (c) shows the critical stretches and composite stress for LOE analysis in the fibers.

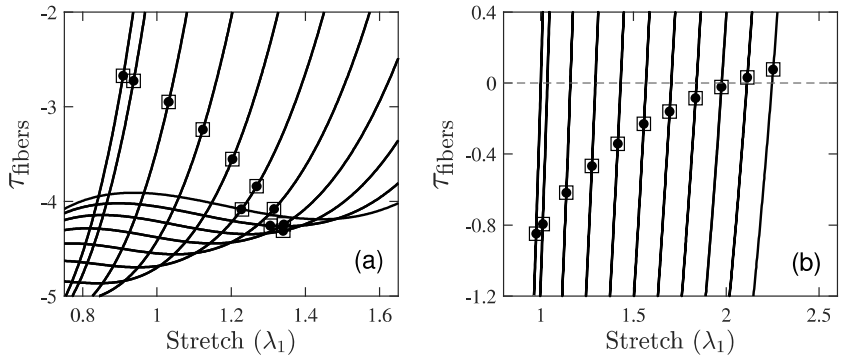

Fig. 8. Stress–stretch curve of the fibers and LOE points for a material with reinforcement modulus $\frac{E_f}{E_m} = 10$ with hardening. (a) shows the critical stretches and fibers stress for LOE analysis in the composite, where the squares with circles inside represent the points of LOE. (b) shows LOE in the fibers.

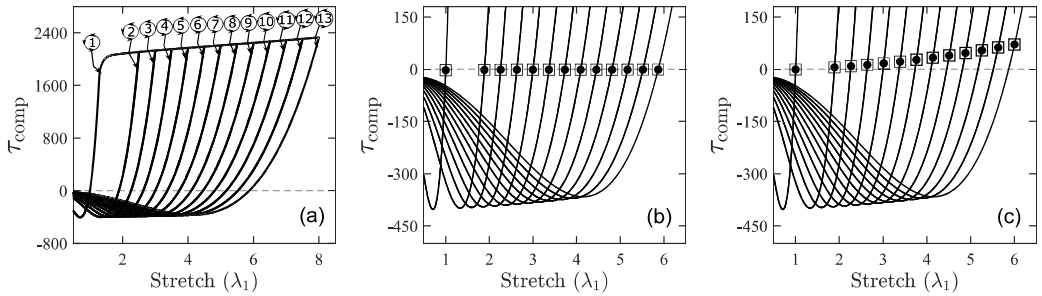

Fig. 9. Stress–stretch curve of the composite and LOE points for a material with reinforcement modulus $\frac{E_f}{E_m} = 1000$ with hardening. (a) shows the 11 loading and unloading steps applied to the material, (b) shows LOE in the composite, where the squares with circles inside represent the points of LOE. (c) shows the critical stretches and composite stress for LOE analysis in the fibers.

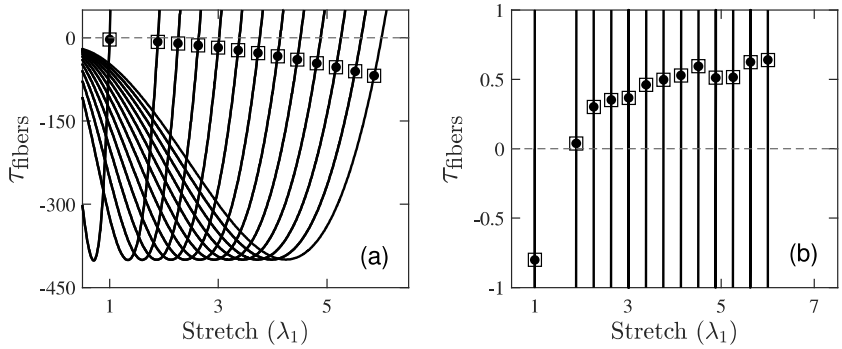

Fig. 10. Stress–stretch curve of the fibers and LOE points for a material with reinforcement modulus $\frac{E_f}{E_m} = 1000$ with hardening. (a) shows the critical stretches and fibers stress for LOE analysis in the composite, where the squares with circles inside represent the points of LOE. (b) shows LOE in the fibers.

Table 2
Critical elastic stretches for each unloading step of a composite with reinforcement $\bar{\kappa} = 10$ with hardening. The second row shows the critical stretches for the LOE analysis in the composite and the third row shows the critical stretches for the ellipticity analysis in the fibers.

$\lambda^{1}_{e,crit}$	Step										
	1	2	3	4	5	6	7	8	9	10	11
LOE comp	0.9084	0.9033	0.8837	0.8586	0.8288	0.7952	0.7566	0.7130	0.6617	0.6020	0.5310
LOE fibers	0.9750	0.9749	0.9749	0.9748	0.9749	0.9752	0.9747	0.9749	0.9749	0.9749	0.9748

Table 3
Critical elastic stretches for each unloading step of a composite with reinforcement $\bar{\kappa} = 1000$ with hardening. The second row shows the critical stretches for the LOE analysis in the composite and the third row shows the critical stretches for the ellipticity analysis in the fibers.

$\lambda^{1}_{e,crit}$	Step												
	1	2	3	4	5	6	7	8	9	10	11	12	13
LOE comp	0.9992	0.9975	0.9966	0.9954	0.9941	0.9926	0.9909	0.9890	0.9870	0.9847	0.9823	0.9797	0.9770
LOE fibers	0.9998	0.9998	0.9998	0.9998	0.9998	0.9998	0.9998	0.9998	0.9998	0.9998	0.9998	0.9998	0.9998

in the direction of the fibers. We perform this study as a means to postulate a mechanism for macroscopic instabilities that emerge in a fashion similar to macroscopic kinking instabilities in tendon. Similar to the phenomenology of tendon kinking, here we show that LOE can arise during elastic unloading (while still in tension) once significant plastic deformation of the fiber phase has taken place. We formulate a material model for the composite by using neo-Hookean strain–energy functions to characterize the constitutive behavior of the phases and the Voigt assumption to approximate the macroscopic constitutive behavior of the composite. In order to analyze the onset of localization in this material, we examine the condition of LOE, which indicates the possibility of onset of localization in a material. We focus both on LOE that can occur in the composite, and in the fiber material. To do so, we formulate an LOE criterion that can be used for an elastoplastic material employing plasticity theory at finite strains based on the multiplicative decomposition of the deformation gradient and hyperelastic laws to characterize the elastic response of the material.

The main insight gained from this work was that LOE can occur under a tensile stress state in the direction of the fibers, and that this effect is caused by plastic deformations of the fibers and the elastic mismatch between the fibers and matrix. An advantage of the Voigt approximation is that it allows obtaining explicit expressions for both the local and the macroscopic incremental modulus tensors in terms of the applied deformation gradient, which in turn simplifies considerably the examination of the associated LOE conditions for the fiber phase and for the composite. Uniquely, we notice that LOE initializes in the fiber phase, but as we do not investigate postbuckling in this study we cannot provide insight on how this localization evolves. We show that, upon cycling that induces plastic deformations in the fiber phase, the LOE occurs in the fiber material for tensile stresses in the composite. This observation proposes a shift in the way we look at the problem of instabilities in soft composite materials since previous studies have been focusing on elastic localizations arising only under compressive loading in the direction of the fibers. These results provide the first mathematical description of the mechanism through which fiber kinking in tendon and ligaments could possibly emanate, emphasizing that plasticity of the fiber components is extremely important for understanding the macroscopic response of biological soft composite tissues. It is important to note that collagen fibers are commonly thought of as not being able to take compressive loads due to their undulated state, but the studies that support this claim focus on individual fibers and neglect the complexity of the microscopic stress state. Here it is suggested, that fiber plasticity can lead to a complex stress state where a tensile state in the matrix and a compressive load in the fibers might exist; this situation is very different than a macroscopic compressive load. Even for undulated fibers, one can think of the fiber–matrix interplay due to the elastic mismatch, as a distributed traction on each fiber bundle that acts as a compressive load, and as an external load that is applied at the ends of the fibers. This key observation is critical towards developing micromechanically accurate models for tendon.

A well-known disadvantage of the Voigt approximation, which has been used in the present work to model the homogenized behavior of the material, is that it accounts for the underlying microstructure only through the volume fractions of the phases. For this reason, it would be interesting to pursue a more detailed homogenization analysis of the instabilities studied in this work and explore the effect of important microstructural features in these composites, including the fiber shape and distribution. As the first step to this end, following the work by Triantafyllidis and Maker (1985) and Nestorović and Triantafyllidis (2004), composite materials with lamellar microstructures may be used as two-dimensional approximations of the actual fiber-reinforced composites of interest. These idealized microstructures are useful not only for studying the critical conditions for the LOE of the homogenized response of composite materials but also for analyzing the stability of their post-bifurcation behavior (d'Avila et al., 2016). Work along these lines is currently under development and will be published in an upcoming study. From the practical point of view in biomechanics, a more important project which is worth pursuing is to develop a predictive model for the mechanical behavior of tendons, incorporating detailed information on the microstructure and on the properties of the constituent phases, which could in turn help shed light on the damage cascade during cyclic loading and overloading in these materials, with the ultimate objective to guide exercise-based treatments for tendinopathy.

CRediT authorship contribution statement

Fernanda F. Fontenele: Methodology, Investigation, Software, Visualization, Writing – original draft, Review & editing. Nelly Andarawis-Puri: Conceptualization, Writing – review & editing. Michalis Agoras: Conceptualization, Supervision, Writing – review & editing. Nikolaos Bouklas: Conceptualization, Supervision, Writing – review & editing, Funding acquisition.

Declaration of competing interest

The authors declare that they have no known competing financial interests or personal relationships that could have appeared to influence the work reported in this paper.

Acknowledgments

The authors gratefully acknowledge fruitful discussions with Professor Nikolaos Aravas. N.A.P, N.B. and F.F. acknowledge the support by the National Science Foundation, USA under grant no. CMMI-2038057.

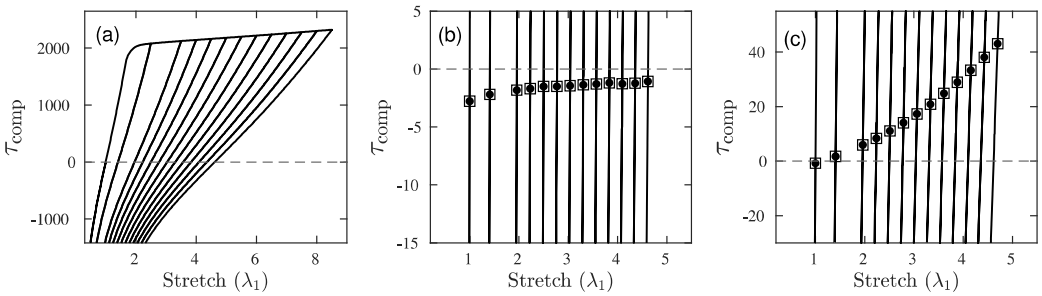

Fig. B.11. Stress–stretch curve of the composite and LOE points for a material with reinforcement modulus = 1000 with hardening for the new energy-function for the fibers (Eq. (B.1)). (a) shows the 13 loading and unloading steps applied to the material, (b) shows LOE in the composite, where the squares with circles inside represent the points of LOE. (c) shows the critical stretches and composite stress for LOE analysis in the fibers.

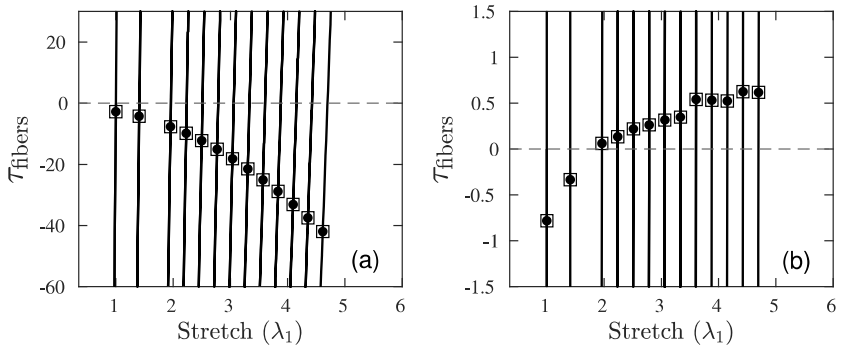

Fig. B.12. Stress–stretch curve of the fibers and LOE points for a material with reinforcement modulus = 1000 with hardening for the new energy-function for the fibers (Eq. (B.1)). (a) shows the critical stretches and fibers stress for LOE analysis in the composite, where the squares with circles inside represent the points of LOE. (b) shows LOE in the fibers.

Appendix A. Thermodynamic limit

In order to examine the thermodynamic stability of the constitutive model, the Drucker stability criterion must be satisfied. The Drucker criterion was first postulated by Hill (1958) and states that the internal work due to mechanical stresses and corresponding deformation of the material can only increase

$$\delta W \cdot \delta \geq 0, \tag{A.1}$$

for elastic materials with no damage mechanisms. This last condition tells us that this criterion holds as long as the stress value increases with an increase in strain, or decreases with a reduction in strain. Triani (2012) established a similar criterion to evaluate the thermodynamic stability of hyperelastic constitutive functions and specialized it to a state of uniaxial deformation in hyperelastic materials as

$$\partial^2 W(I_t)/\partial I_t^{\,2} \geq 0, \tag{A.2}$$

where W is the energy function characterizing the elastic response of the material and I_t denotes, in this equation, the stretch in the direction of the applied uniaxial load. Since the $\partial^2 W(I_t)/\partial I_t^{\,2}$ represents the sign of the slope in the stress–stretch curve, this condition tells us that any change in the stress should result in a change in the strain of the same sign, thus yielding essentially the same criterion as (A.1), however in terms of the strain–energy function.

We examine the elastic loading/unloading material response prior to yielding (=) under uniaxial loading in the direction of the fibers (which corresponds to the condition = 0 for $_3$, $_4 \neq 1$, 1 in this work). We do that by taking the energy function of the fibers in (48), computing the Kirchhoff stress of the fibers using (34), and then calculating ∂ / ∂ $_{11}$ to check for the thermodynamic condition, following (A.2). We, therefore, check if ∂ / ∂ $_{11} \geq 0$ holds at all times or if there is such a range of stretch values at which the constitutive behavior violates the Drucker stability criterion.

Appendix B. A thermodynamically stable strain–energy function for the fiber phase

The strain–energy function used in this work to represent the fiber phase in (48) reaches a thermodynamic limit (discussed in Appendix A) during compressive loading for values of reinforcement that are large enough. Here, we check the validity of our calculations reported in Section 5 by changing the constitutive model of the fiber phase to the following strain–energy function

$$W^{fiber}_{fine}(\bar{I}_1) = \frac{}{2}(\bar{I}_1 - 3) - 2\ln J + \frac{}{2}(J^2 - 1) + \frac{}{2}\left(\bar{I}_4 + \frac{2}{\bar{I}_4} - 3\right), \tag{B.1}$$

which has the advantage of satisfying the thermodynamic limitations for all possible deformations. It is remarked that in the incompressibility limit $J \to 1$, the above expression takes the form of the homogenized strain–energy function determined by DeBotton et al. (2006) for a fiber-reinforced composite with neo-Hookean constituents. It is also remarked that only the reinforcement term for the fiber phase is modified, while the energy-function of the matrix in (47) is kept unchanged. We follow the same kinematics, plasticity and loss of ellipticity formulation described throughout this paper, and we plot the same set of results as in Section 5.2 for the reinforcement modulus of = 1000 in Figs. B.11–B.12.

Essentially, the trends of results remain the same as for the results generated from the energy-function used for the fibers throughout this work (48) when this last one is restricted to the physically admissible range of the energy function, before the thermodynamic limit is reached. From Fig. B.11, we verify that, as reported in Section 5, loss of ellipticity calculated in the fiber phase occurs prior to the loss of ellipticity in the composite and that the loss of ellipticity of the fibers can occur when the material is under tensile state (Fig. 11(c)). Loss of ellipticity is also found either during elastic unloading or elastic compressive loading.

References

Agoras, M., Lopez-Pamies, O., Castañeda, P.P., 2009a. A general hyperelastic model for incompressible fiber-reinforced elastomers. J. Mech. Phys. Solids 57 (2), 268–286.

Agoras, M., Lopez-Pamies, O., Castañeda, P.P., 2009b. Onset of macroscopic instabilities in fiber-reinforced elastomers at finite strain. J. Mech. Phys. Solids 57 (11), 1828–1850.

Andarawis-Puri, N., Flatow, E., 2011. Tendon fatigue in response to mechanical loading. J. Musculoskelet. Neuronal Interact. 11 (2), 106.

Andarawis-Puri, N., Flatow, E.L., Soslowsky, L.J., 2015. Tendon basic science: Development, repair, regeneration, and healing. J. Orthop. Res. 33 (6), 780–784.

Andarawis-Puri, N., Ricchetti, E.T., Soslowsky, L.J., 2009. Rotator cuff tendon strain correlates with tear propagation. J. Biomech. 42 (2), 158–163.

Andarawis-Puri, N., Sereysky, J.B., Jepsen, K.J., Flatow, E.L., 2012a. The relationships between cyclic fatigue loading, changes in initial mechanical properties, and the in vivo temporal mechanical response of the rat patellar tendon. J. Biomech. 45 (1), 59–65.

Andarawis-Puri, N., Sereysky, J.B., Sun, H.B., Jepsen, K.J., Flatow, E.L., 2012b. Molecular response of the patellar tendon to fatigue loading explained in the context of the initial induced damage and number of fatigue loading cycles. J. Orthop. Res. 30 (8), 1327–1334.

Ansari, F., Galland, S., Johansson, M., Plummer, C.J., Berglund, L.A., 2014. Cellulose nanofiber network for moisture stable, strong and ductile biocomposites and increased epoxy curing rate. Composites A 63, 35–44.

Aravas, N., 1994. Finite-strain anisotropic plasticity and the plastic spin. Modelling Simulation Mater. Sci. Eng. 2 (3A), 483.

Baldwin, S.J., Kreplak, L., Lee, J.M., 2016. Characterization via atomic force microscopy of discrete plasticity in collagen fibrils from mechanically overloaded tendons: Nano-scale structural changes mimic rope failure. J. Mech. Behav. Biomed. Mater. 60, 356–366.

Baldwin, S.J., Quigley, A.S., Clegg, C., Kreplak, L., 2014. Nanomechanical mapping of hydrated rat tail tendon collagen I fibrils. Biophys. J. 107 (8), 1794–1801.

Beese, A.M., Sarkar, S., Nair, A., Naraghi, M., An, Z., Moravsky, A., Loutfy, R.O., Buehler, M.J., Nguyen, S.T., Espinosa, H.D., 2013. Bio-inspired carbon nanotube–polymer composite yarns with hydrogen bond-mediated lateral interactions. ACS Nano 7 (4), 3434–3446.

Berbinau, P., Soutis, C., Goutas, P., Curtis, P., 1999. Effect of off-axis ply orientation on 0-fibre microbuckling. Composites A 30 (10), 1197–1207.

Bosia, F., Buehler, M.J., Pugno, N.M., 2010. Hierarchical simulations for the design of supertough nanofibers inspired by spider silk. Phys. Rev. E 82 (5), 056103.

Budiansky, B., Fleck, N.A., 1993. Compressive failure of fibre composites. J. Mech. Phys. Solids 41 (1), 183–211.

Budiansky, B., Fleck, N.A., 1994. Compressive kinking of fiber composites: a topical review.

Burla, F., Dussi, S., Martinez-Torres, C., Tauber, J., van der Gucht, J., Koenderink, G.H., 2020. Connectivity and plasticity determine collagen network fracture. Proc. Natl. Acad. Sci. 117 (15), 8326–8334.

Callens, M., Gorbatikh, L., Verpoest, I., 2014. Ductile steel fibre composites with brittle and ductile matrices. Composites A 61, 235–244.

Cheung, H.-Y., Lau, K.-T., Tao, X.-M., Hui, D., 2008. A potential material for tissue engineering: Silkworm silk/pla biocomposite. Composites B 39 (6), 1026–1033.

Ciarletta, P., Ben Amar, M., 2009. A finite dissipative theory of temporary interfibrillar bridges in the extracellular matrix of ligaments and tendons. J. R. Soc. Interface 6 (39), 909–924.

Ciarletta, P., Dario, P., Micera, S., 2008. Pseudo-hyperelastic model of tendon hysteresis from adaptive recruitment of collagen type I fibrils. Biomaterials 29 (6), 764–770.

d'Avila, M.S., Triantafyllidis, N., Wen, G., 2016. Localization of deformation and loss of macroscopic ellipticity in microstructured solids. J. Mech. Phys. Solids 97, 275–298.

DeBotton, G., Hariton, I., Socolsky, E., 2006. Neo-hookean fiber-reinforced composites in finite elasticity. J. Mech. Phys. Solids 54 (3), 533–559.

Ericksen, J.L., Rivlin, R.S., 1954. Large elastic deformations of homogeneous anisotropic materials. Indiana Univ. Math. J. 3, 467–487.

Fleck, N., 1997. Compresssive failure of fiber composites. Adv. Appl. Mech. 33 (6), 7.

Freedman, B.R., Gordon, J.A., Soslowsky, L.J., 2014. The achilles tendon: fundamental properties and mechanisms governing healing. Muscles, Ligaments Tendons J. 4 (2), 245.

Fung, D.T., Wang, V.M., Andarawis-Puri, N., Basta-Pljakic, J., Li, Y., Laudier, D.M., Sun, H.B., Jepsen, K.J., Schaffler, M.B., Flatow, E.L., 2010. Early response to tendon fatigue damage accumulation in a novel in vivo model. J. Biomech. 43 (2), 274–279.

Fung, D.T., Wang, V.M., Laudier, D.M., Shine, J.H., Basta-Pljakic, J., Jepsen, K.J., Schaffler, M.B., Flatow, E.L., 2009. Subrupture tendon fatigue damage. J. Orthop. Res. 27 (2), 264–273.

Furer, J., Castañeda, P.P., 2020. Reinforced elastomers: Homogenization, macroscopic stability and relaxation. J. Mech. Phys. Solids 136, 103689.

Gasser, T.C., Holzapfel, G.A., 2002. A rate-independent elastoplastic constitutive model for biological fiber-reinforced composites at finite strains: continuum basis, algorithmic formulation and finite element implementation. Comput. Mech. 29 (4–5), 340–360.

Gea, S., Bilotti, E., Reynolds, C.T., Soykeabkeaw, N., Peijs, T., 2010. Bacterial cellulose–poly (vinyl alcohol) nanocomposites prepared by an in-situ process. Mater. Lett. 64 (8), 901–904.

Geymonat, G., Müller, S., Triantafyllidis, N., 1993. Homogenization of nonlinearly elastic materials, microscopic bifurcation and macroscopic loss of rank-one convexity. Arch. Ration. Mech. Anal. 122 (3), 231–290.

Guo, Z., Peng, X., Moran, B., 2007. Mechanical response of neo-hookean fiber reinforced incompressible nonlinearly elastic solids. Int. J. Solids Struct. 44 (6), 1949–1969.

Herod, T.W., Chambers, N.C., Veres, S.P., 2016. Collagen fibrils in functionally distinct tendons have differing structural responses to tendon rupture and fatigue loading. Acta Biomater. 42, 296–307.

Hill, R., 1958. A general theory of uniqueness and stability in elastic-plastic solids. J. Mech. Phys. Solids 6 (3), 236–249.

Hill, R., 1972. On constitutive macro-variables for heterogeneous solids at finite strain. Proc. R. Soc. Lond. Ser. A Math. Phys. Eng. Sci. 326 (1565), 131–147.

Jozsa, L., Balint, B., Reffy, A., Demel, Z., 1984. Fine structural alterations of collagen fibers in degenerative tendinopathy. Arch. Orthop. Trauma. Surg. 103 (1), 47–51.

Kyriakides, S., Arseculeratne, R., Perry, E., Liechti, K., 1995. On the compressive failure of fiber reinforced composites. Int. J. Solids Struct. 32 (6–7), 689–738.

Larsson, P.A., Berglund, L.A., Wagberg, L., 2014. Ductile all-cellulose nanocomposite films fabricated from core–shell structured cellulose nanofibrils. Biomacromolecules 15 (6), 2218–2223.

Lee, E.H., 1969. Elastic-plastic deformation at finite strains.

Lee, H.-J., Chung, T.-J., Kwon, H.-J., Kim, H.-J., Tze, W.T.Y., 2012. Fabrication and evaluation of bacterial cellulose-polyaniline composites by interfacial polymerization. Cellulose 19 (4), 1251–1258.

Li, G., Meng, H., Hu, J., 2012. Healable thermoset polymer composite embedded with stimuli-responsive fibres. J. R. Soc. Interface 9 (77), 3279–3287.

Li, Y., Zhou, B., Zheng, G., Liu, X., Li, T., Yan, C., Cheng, C., Dai, K., Liu, C., Shen, C., et al., 2018. Continuously prepared highly conductive and stretchable SWNT/MWNT synergistically composited electrospun thermoplastic polyurethane yarns for wearable sensing. J. Mater. Chem. C 6 (9), 2258–2269.

Liu, I.-S., 2012. A note on the mooney–rivlin material model. Contin. Mech. Thermodyn. 24 (4–6), 583–590.

Maffulli, N., Wong, J., Almekinders, L.C., 2003. Types and epidemiology of tendinopathy. Clin. Sports Med. 22 (4), 675–692.

Mandel, J., 1971. ''Plasticite classique et viscoplasticite'' Nummer 97 in Courses and Lectures. Springer, New York, International Centre for Mechanical Sciences, Udine.

Merodio, J., Ogden, R., 2002. Material instabilities in fiber-reinforced nonlinearly elastic solids under plane deformation. Arch. Mech. 54 (5–6), 525–552.

Merodio, J., Ogden, R., 2003. Instabilities and loss of ellipticity in fiber-reinforced compressible non-linearly elastic solids under plane deformation. Int. J. Solids Struct. 40 (18), 4707–4727.

Natali, A., Pavan, P., Carniel, E., Lucisano, M., Taglialavoro, G., 2005. Anisotropic elasto-damage constitutive model for the biomechanical analysis of tendons. Med. Eng. Phys. 27 (3), 209–214.

Nestorović, M., Triantafyllidis, N., 2004. Onset of failure in finitely strained layered composites subjected to combined normal and shear loading. J. Mech. Phys. Solids 52 (4), 941–974.

Neviaser, A., Andarawis-Puri, N., Flatow, E., 2012. Basic mechanisms of tendon fatigue damage. J. Shoulder Elb. Surg. 21 (2), 158–163.

Pan, L., Wang, F., Cheng, Y., Leow, W.R., Zhang, Y.-W., Wang, M., Cai, P., Ji, B., Li, D., Chen, X., 2020. A supertough electro-tendon based on spider silk composites. Nature Commun. 11 (1), 1–9.

Pereda, J., Aravas, N., Bassani, J., 1993. Finite deformations of anisotropic polymers. Mech. Mater. 15, 3–20.

Qiu, G., Pence, T., 1997a. Loss of ellipticity in plane deformation of a simple directionally reinforced incompressible nonlinearly elastic solid. J. Elasticity 49 (1), 31–63.

Qiu, G., Pence, T., 1997b. Remarks on the behavior of simple directionally reinforced incompressible nonlinearly elastic solids. J. Elasticity 49 (1), 1–30.

Renardy, M., Rogers, R.C., 2004. An Introduction to Partial Differential Equations. vol. 13, Springer Science & Business Media.

Rice, J.R., 1976. Localization of plastic deformation. Technical Report, Brown Univ., Providence RI (USA). Div. of Engineering.

Rosen, B.W., 1965. Mechanics of composite strengthening.

Rudnicki, J.W., Rice, J., 1975. Conditions for the localization of deformation in pressure-sensitive dilatant materials. J. Mech. Phys. Solids 23 (6), 371–394.

Sehaqui, H., Zhou, Q., Berglund, L.A., 2011. Nanostructured biocomposites of high toughness—a wood cellulose nanofiber network in ductile hydroxyethylcellulose matrix. Soft Matter 7 (16), 7342–7350.

Shen, Z.L., Dodge, M.R., Kahn, H., Ballarini, R., Eppell, S.J., 2010. In vitro fracture testing of submicron diameter collagen fibril specimens. Biophys. J. 99 (6), 1986–1995.

Sivashanker, S., Fleck, N., Sutcliffe, M., 1996. Microbuckle propagation in a unidirectional carbon fibre-epoxy matrix composite. Acta Mater. 44 (7), 2581–2590.

Spencer, A.J.M., 1984. Constitutive theory for strongly anisotropic solids. In: Continuum Theory of the Mechanics of Fibre-Reinforced Composites. Springer, pp. 1–32.

Sun, C., Chen, J., 1989. A simple flow rule for characterizing nonlinear behavior of fiber composites. J. Compos. Mater. 23 (10), 1009–1020.

Szczesny, S.E., Peloquin, J.M., Cortes, D.H., Kadlowec, J.A., Soslowsky, L.J., Elliott, D.M., 2012. Biaxial tensile testing and constitutive modeling of human supraspinatus tendon. J. Biomech. Eng. 134 (2).
Tang, Y., Ballarini, R., Buehler, M.J., Eppell, S.J., 2010. Deformation micromechanisms of collagen fibrils under uniaxial tension. J. R. Soc. Interface 7 (46), 839–850.
Thorpe, C.T., Screen, H.R., 2016. Tendon structure and composition. In: Metabolic Influences on Risk for Tendon Disorders. Springer, pp. 3–10.
Tiel, J.v., 1984. Convex Analysis (BOOK). John Wiley.
Triantafyllidis, N., Abeyaratne, R., 1983. Instabilities of a finitely deformed fiber-reinforced elastic material.
Triantafyllidis, N., Maker, B., 1985. On the comparison between microscopic and macroscopic instability mechanisms in a class of fiber-reinforced composites.
Veres, S.P., Brennan-Pierce, E.P., Lee, J.M., 2015. Macrophage-like U937 cells recognize collagen fibrils with strain-induced discrete plasticity damage. J. Biomed. Mater. Res. Part A 103 (1), 397–408.
Veres, S.P., Harrison, J.M., Lee, J.M., 2013. Repeated subrupture overload causes progression of nanoscaled discrete plasticity damage in tendon collagen fibrils. J. Orthop. Res. 31 (5), 731–737.
Veres, S.P., Harrison, J.M., Lee, J.M., 2014. Mechanically overloading collagen fibrils uncoils collagen molecules, placing them in a stable denatured state. Matrix Biol. 33, 54–59.
Vogler, T., Hsu, S.-Y., Kyriakides, S., 2000. Composite failure under combined compression and shear. Int. J. Solids Struct. 37 (12), 1765–1791.
Wang, S., Jiang, F., Xu, X., Kuang, Y., Fu, K., Hitz, E., Hu, L., 2017. Super-strong, super-stiff macrofibers with aligned, long bacterial cellulose nanofibers. Adv. Mater. 29 (35), 1702498.
Wu, R., Ma, L., Hou, C., Meng, Z., Guo, W., Yu, W., Yu, R., Hu, F., Liu, X.Y., 2019. Silk composite electronic textile sensor for high space precision 2d combo temperature–pressure sensing. Small 15 (31), 1901558.
Yodmuang, S., McNamara, S.L., Nover, A.B., Mandal, B.B., Agarwal, M., Kelly, T.-A.N., Chao, P.-h.G., Hung, C., Kaplan, D.L., Vunjak-Novakovic, G., 2015. Silk microfiber-reinforced silk hydrogel composites for functional cartilage tissue repair. Acta Biomater. 11, 27–36.